VOLUME 63 JOURNAL OF APPLIED METEOROLOGY AND CLIMATOLOGY JANUARY 2024

Investigation of Hydrostatic Imbalance with Field Observations

JIELUN SUN,[a] VOLKER WULFMEYER,[b] FLORIAN SPÄTH,[b] HOLGER VÖMEL,[c] WILLIAM BROWN,[c]
AND STEVEN ONCLEY[c]

[a] *NorthWest Research Associates, Boulder, Colorado*
[b] *Institute of Physics and Meteorology, University of Hohenheim, Stuttgart, Germany*
[c] *National Center for Atmospheric Research, Boulder, Colorado*

(Manuscript received 27 December 2022, in final form 30 July 2023, accepted 26 September 2023)

ABSTRACT: The hydrostatic equilibrium addresses the approximate balance between the positive force of the vertical pressure gradient and the negative gravity force and has been widely assumed for atmospheric applications. The hydrostatic imbalance of the mean atmospheric state for the acceleration of vertical motions in the vertical momentum balance is investigated using tower, the global positioning system radiosonde, and Doppler lidar and radar observations throughout the diurnally varying atmospheric boundary layer (ABL) under clear-sky conditions. Because of the negligibly small mean vertical velocity, the acceleration of vertical motions is dominated by vertical variations of vertical turbulent velocity variances. The imbalance is found to be mainly due to the vertical turbulent transport of changing air density as a result of thermal expansion/contraction in response to air temperature changes following surface temperature changes. In contrast, any pressure change associated with air temperature changes is small, and the positive vertical pressure-gradient force is strongly influenced by its background value. The vertical variation of the turbulent velocity variance from its vertical increase in the lower convective boundary layer (CBL) to its vertical decrease in the upper CBL is observed to be associated with the sign change of the imbalance from positive to negative due to the vertical decrease of the positive vertical pressure-gradient force and the relative increase of the negative gravity force as a result of the decreasing upward transport of the low-density air. The imbalance is reduced significantly at night but does not steadily approach zero. Understanding the development of hydrostatic imbalance has important implications for understanding large-scale atmosphere, especially for cloud development.

SIGNIFICANCE STATEMENT: It is well known that the hydrostatic imbalance between the positive pressure-gradient force due to the vertical decrease of atmospheric pressure and the negative gravity forces in the vertical momentum balance equation has important impacts on the vertical acceleration of atmospheric vertical motions. Vertical motions for mass, momentum, and energy transfers contribute significantly to changing atmospheric dynamics and thermodynamics. This study investigates the often-assumed hydrostatic equilibrium and investigate how the hydrostatic imbalance is developed using field observations in the atmospheric boundary layer under clear-sky conditions. The results reveal that hydrostatic imbalance can develop from the large-eddy turbulent transfer of changing air density in response to the surface diabatic heating/cooling. The overwhelming turbulence in response to large-scale thermal forcing and mechanical work of the vast Earth surface contributes to the hydrostatic imbalance on large spatial and temporal scales in numerical weather forecast and climate models.

KEYWORDS: Atmosphere–land interaction; Momentum; In situ atmospheric observations; Lidars/lidar observations; Radars/radar observations; Radiosonde/rawinsonde observations

1. Introduction

The hydrostatic imbalance is the imbalance between the positive pressure-gradient force from decreasing atmospheric pressure with height $-\partial p/\partial z$ and the negative gravity force $-\rho g$ in the vertical momentum balance for the atmosphere where p, ρ, z, and g are air pressure and density, the height above the surface, and gravity acceleration, respectively. The hydrostatic imbalance regardless of its magnitude drives acceleration of vertical motions. Nonhydrostatic processes are investigated, for example, in gravity waves (e.g., Eliassen and Palm 1960; Smith 1979), detrainment vertical transport of condensed water content and aerosols by deep convection (e.g., Xue et al. 2000; Cotton et al. 2010), and frontal bands (e.g., Dudhia 1993). Weather events due to the hydrostatic imbalance have been investigated extensively in the atmosphere research community mainly through numerical models for cloud development (e.g., Xue et al. 2000). Buoyancy between clear and cloudy areas is considered to contribute to the mass flux for deep convection in the vertical momentum balance (e.g., Kuo 1974; Donner 1993). Boundary layer shallow cumulus clouds are commonly described through the sum of eddy diffusion and mass flux (e.g., Soares et al. 2004; Siebesma et al. 2007; Angevine et al. 2010). Nonhydrostatic models often include air compressibility and pressure changes associated with acoustic waves, which are often dealt with by applying anelastic equations (e.g., Arakawa and Konor 2009; Cotton

---

Denotes content that is immediately available upon publication as open access.

Späth's current affiliation: Institute of Soil Science and Land Evaluation, Biogeophysics, University of Hohenheim, Stuttgart, Germany.

Corresponding author: Jielun Sun, jielun@nwra.com

DOI: 10.1175/JAMC-D-22-0206.1

et al. 2010). The widely used validation for nonhydrostatic models is done through comparison with the numerical study of density currents by Straka et al. (1993). With increasing computing power and model resolution, regional and global climate models are approaching resolving clouds (e.g., Skamarock and Klemp 2008; Arakawa and Konor 2009; Skamarock et al. 2012; Satoh 2014; Prein et al. 2015; Taylor et al. 2020). Nonhydrostatic processes have drawn increasing attention for addressing cloud processes and aerosol–cloud impacts on climate change (e.g., Arakawa 2004; Stephens 2005).

The hydrostatic imbalance is a mechanical force responsible for the acceleration of vertical motions. For a two-dimensional airflow with the horizontal wind V in the direction of x and the vertical velocity w in z, the vertical momentum balance with the good approximation of the continuity equation can be expressed as (e.g., Stull 1988; Garratt 1992; Sun 2019)

$$\rho\left(\frac{\partial w}{\partial t} + \frac{\partial wV}{\partial x} + \frac{\partial w^2}{\partial z}\right) = -\left(\frac{\partial p}{\partial z} + \rho g\right) + \mu\left(\frac{\partial^2 w}{\partial x^2} + \frac{\partial^2 w}{\partial z^2}\right), \qquad (1)$$

where μ represents the air dynamic viscosity due to molecule collisions with different speeds. In the atmosphere, the rate of vertical momentum change per unit volume $\rho dw/dt$ (kg $\mathrm{m}^{-2}\ \mathrm{s}^{-2}$) is driven by the hydrostatic imbalance force $-(\partial p/\partial z + \rho g)$ and the air viscous force due to air motions and air viscosity [the last term in Eq. (1)]. Because the viscous force consumes environmental momentum for cascading energetic large turbulent eddies down to small ones, the driving force for the w acceleration is the hydrostatic imbalance force. The hydrostatic imbalance force relies on the delicate imbalance between the positive vertical pressure-gradient force $-\partial p/\partial z$ and the negative gravity force $-\rho g$.

Atmospheric vertical motions include not only mean but also turbulent vertical motions. Identifying the role of mean and turbulent motions in Eq. (1) can be achieved by first decomposing each variable ϕ as $\phi = \overline{\phi} + \phi'$, where $\overline{\phi}$ is the Reynolds-averaged ϕ and ϕ' represents the turbulent perturbation of ϕ relative to $\overline{\phi}$, and then Reynolds averaging the decomposed Eq. (1). Clearly, the so-called turbulent motion represents any air motion with scale less than the Reynolds averaging scale. There is no clear physical division between turbulent and mesoscale motions. Because the Reynolds average is a simple box average, $\overline{\phi'} = 0$. Reynolds averaging the decomposed Eq. (1) with the assumptions of $|\rho'/\overline{\rho}| \ll 1$, $|\partial p'/\partial z| \ll |\partial\overline{p}/\partial z|$ (see section 3c for characteristics of turbulent mixing), and the horizontal homogeneity of the surface and the ambient flow (i.e., $\partial\overline{\phi}/\partial x = 0$), Eq. (1) can be simplified as (see the appendix)

$$\overline{\rho}\left(\frac{\partial\overline{w}}{\partial t} + \frac{\partial\overline{w'^2}}{\partial z}\right) \approx -\left(\frac{\partial\overline{p}}{\partial z} + \overline{\rho}g\right) + \mu\left(\frac{\partial^2\overline{w}}{\partial z^2} - \frac{1}{\overline{\rho}}\overline{\rho'\frac{\partial^2 w'}{\partial z^2}}\right). \qquad (2)$$

A large body of turbulence work in the literature is on small turbulent eddies. Here small turbulent eddies or local turbulent eddies refer to those for which their turbulent transfer of a scalar at a location is related to the local gradient of the scalar at the point in analogy to molecular diffusion (e.g., Stull 1993). However, the most energetic turbulent eddies are generated by environmental forcing, particularly the vertical forcing of environmental flows such as mechanical work due to vertical wind shear or positive buoyancy from surface heating. Environmental forcing here is used to represent ambient energy sources in general. Recently, Sun et al. (2012, 2016, 2020) demonstrated that the most energetic turbulent eddies in the atmospheric boundary layer (ABL), which contribute to the maximum value of vertical velocity oscillations in vertical velocity power spectra, have the characteristic finite vertical scale of the environmental forcing in the atmosphere. Thus, the most energetic turbulent eddies are not related to small-spatial-scale local gradients and are nonlocal large turbulent eddies. The usage of "nonlocal" eddies here is consistent with its usage in the literature for distinguishing them from local or small turbulent eddies and does not imply the origin of turbulence generation. In this study, we refer to turbulent eddies that are related to local gradients as small ones, and other ones are large ones.

Turbulent mixing generated by large-scale environmental forcing is much stronger and more effective than molecular diffusion from random molecule motions in transferring mass, momentum, and energy. With the reduced impact of the ground surface, the vertical scale of the environmental forcing increases with height so does the vertical scale of the most energetic turbulent eddies. Therefore, vertical momentum and energy transfers by the most energetic large turbulent eddies can effectively influence atmospheric dynamics and thermodynamics over a large range of scales. Early cloud observations have led to the proposed "bubble" concept for cumulus convection (e.g., Ooyama 1971), which resembles a group of large turbulent eddies. The mass-flux contribution to convection discussed in the literature (e.g., Soares et al. 2004) could be essentially the energy transfer by relatively large turbulent eddies under diabatic heating conditions. In contrast to large nonlocal energetic turbulent eddies, small eddies that cascade down from these energetic ones as a result of air viscosity and angular deformation from wind shear contribute much less to vertical mass, momentum, and energy transfers.

Large nonlocal turbulent mixing has been investigated in laboratories and through numerical models (e.g., Adrian et al. 1986; Stull 1988, 1993; Hutchins et al. 2012; Pandey et al. 2018). Large turbulent eddies near the ground have also been investigated as attached wall eddies (e.g., Townsend 1976; Krug et al. 2019; Marusic and Monty 2019; Li et al. 2022), or "inactive eddies" (e.g., Bradshaw 1967; Högström 1990). Because the dominant role of large turbulent eddies in the turbulent transfer of any scalar, turbulent mixing of any scalar is not related to local vertical gradients of the scalar. Parameterizing observed large-eddy turbulent fluxes with local gradients would sometimes require "countergradient fluxes" (e.g., Edwards et al. 2020) for correcting misrepresentation of relatively large-scale turbulent eddies with small-scale local gradients. Countergradient fluxes under convective conditions are sometimes addressed through convective mass fluxes by thermal plumes (e.g., Siebesma and Cuijpers 1995; Olson et al. 2019; Angevine et al. 2020), which have been traditionally used for cumulus convection development (e.g., Donner 1993).

The latest understanding of energetic large-eddy vertical mass, momentum, and energy transfers has strong implications for contribution of turbulence to the hydrostatic imbalance of the atmosphere and interactions of air motions across scales. Fundamentally, the same physics laws govern atmospheric dynamics and thermodynamics regardless of their temporal and spatial scales. To our knowledge, turbulent momentum and energy transfers have been considered in current nonhydrostatic models but have not been investigated for their contribution to the hydrostatic imbalance. The crucial knowledge gap regarding hydrostatic imbalance is to understand how the hydrostatic imbalance is developed in the atmosphere.

This study focuses on this important knowledge gap by investigating development of the hydrostatic imbalance using field observations in the ABL. Because of visibly large vertical turbulent motions in the ABL, hydrostatic imbalance in the ABL is expected. However, how the hydrostatic imbalance is physically developed, whether the physical process for establishing the hydrostatic imbalance impacts large-scale motions, and what possible physical processes leading to the hydrostatic equilibrium remain unclear as far as we know. Using the field observations described in section 2, we investigate physical development of the hydrostatic imbalance of the mean atmospheric state using in situ tower observations at the bottom of the ABL in section 3 and using both in situ and remote sensing data throughout the ABL in section 4. The main results and conclusions as well as implications of contribution of large-eddy turbulent mixing to large-scale hydrostatic imbalance are summarized in section 5.

2. Field observations and data analysis methods

a. In situ tower observations

In situ tower observations used in this study were collected during the Cooperative Atmosphere-Surface Exchange Study in 1999 (CASES-99) (UCAR/NCAR Earth Observing Laboratory 2016), which was conducted in southeastern Kansas during October 1999. The CASES-99 land surface was covered with dominant short senescent grass of about 0.1 m tall over a relatively flat land (Poulos et al. 2002; Sun et al. 2002, 2003, 2013). There was a 60-m tower in the center surrounded by six stations within 300 m from the 60-m tower. On the 60-m tower, there were eight three-dimensional sonic anemometers (Campbell Scientific, Inc., CSAT, version 3). The top seven levels were 5, 10, 20, 30, 40, 50, and 55 m above the surface, and the lowest one was at 1.5 and 0.5 m before and after 20 October, respectively, for investigating vertical variations of the surface layer. Air temperature was measured at 5 samples per second with thermocouples (E-type, Chromel/Costantan) at 34 levels with the vertical resolution of 1.8 m from 2.3 to 58.1 m on the 60-m tower, and at 0.2 and 0.6 m on two adjacent poles about 1 m from the 60-m tower (Burns and Sun 2000; Sun et al. 2002). Because of the small diameter and the material of the thermocouple sensors, the radiation error of less than 0.1 K is expected based on the study of Foken (2017, their Fig. 6.16). Paroscientific pressure sensors with a resolution of 0.2 Pa were sampled at every 2 s^{-1} and were collocated with the sonic anemometers at the lowest level (0.5 or 1.5 m), 30 m, and 50 m on the 60-m tower (Cuxart et al. 2002). The horizontal separation distance between the sonic anemometer and the pressure sensor at each level was about 0.2–0.3 m. A narrowband infrared (IR) radiometer manufactured by Everest Interscience, Inc., for measuring surface skin temperature was mounted at a vertical angle of 45° on each tower at the six stations. The incoming and outgoing shortwave radiation were measured at station 2, which is about 100 m from the 60-m tower. Krypton hygrometers (Campbell Scientific KH-20) for measuring moisture fluctuations were at 5, 20, 40, and 55 m. Aspirated Vaisala, Inc., 50Y Humitter sensors [platinum resistance thermometers (PRTs)] for temperature/humidity measurements were installed at 5, 15, 25, 35, 45, and 55 m on the 60-m tower as well as at 2 and 10 m at each of the six stations.

b. Doppler lidar observations

Wind measurements with Doppler lidars manufactured by Halo Photonics, Ltd. were obtained at the long-term Land–Atmosphere Feedback Observatory (LAFO) operated by the University of Hohenheim in southwest Germany (Wulfmeyer et al. 2020; Späth et al. 2023a). The LAFO site consists of agricultural fields with small elevation changes between 390 and 420 m over an area of 0.84 km^2. The Doppler lidars observations are based on the coherent detection technique with high-resolution line-of-sight wind measurements and cover the bottom atmosphere up to about 4 km with the velocity precision of less than 0.2 m s^{-1} according to the Halo Photonics website. The temporal and spatial resolutions for the lidar data used in this study are 10 s and 15 m for vertical velocity and 90 s and 21 m for horizontal wind (Späth et al. 2023b).

c. GPS radiosonde observations

Radiosonde observations using the global positioning system (GPS) collected at Rogers Memorial Farm, Nebraska, during the field campaign, Great Plains Irrigation Experiments (GRAINEX) (UCAR/NCAR Earth Observing Laboratory 2018; Rappin et al. 2021) are also used to examine the hydrostatic imbalance in this study. Vaisala RS41-SGP radiosondes processed by the Vaisala MW41 sounding system (version 2.5.0) were deployed during GRAINEX (Vömel and Brown 2018). Sonde altitude and pressure are independently measured using satellite ranging codes with differential corrections from the MW41 ground station and the silicon capacitor pressure sensor, respectively. The sounding reacquisition time for GPS receivers is 1 s. The pressure resolution is 0.01 hPa. The manufacture accuracy for the pressure measurement is smaller than 0.5 hPa. The absolute accuracy for GPS position values is about ±5 m. Additionally, downward solar radiation at 1 m above the surface measured by a Hukseflux radiometer is used to select sunny convective days in this study.

d. Doppler radar wind observations

During GRAINEX, a Vaisala LAP3000 915-MHz boundary layer Doppler Beam Swing (DBS) radar wind profiler (UCAR/NCAR Earth Observing Laboratory 2021) based on the early technology developed by NOAA/Aeronomy Laboratory in the 1990s (Ecklund et al. 1990) was deployed at Rogers Memorial Farm as well. Vertical velocity using LapXM hardware and software was calculated from raw Doppler spectra data with spectral moments averaged over 30 min and postprocessed to remove artifacts such as clutter, interference, and aliasing (Morse et al. 2002).

e. Field data processing

For tower data analysis, we only concentrate on the bottom 30-m layer. All the observations are averaged over 5-min intervals including turbulent fluxes. All the turbulent fluxes are calculated using the eddy correlation method with 5-min block averaging as the 5-min dataset approximately captures the most energetic eddies in this layer. The decrease of the scale of the most energetic eddies toward the surface is demonstrated in the lidar data analysis in section 4a.

We use the pressure measurements at the lowest two levels, 1.5/0.5 and 30 m, to estimate mean vertical pressure variations within the bottom 30-m air layer. Turbulent pressure fluxes are estimated using the pressure and sonic anemometer measurements collocated at 1.5/0.5 and 30 m and sampled at 1 s^{-1}. Because turbulent mixing during daytime and under strong winds is dominated by the most energetic large turbulence eddies (e.g., Sun et al. 2020), the 1 s^{-1} sampling rate would be sufficient for capturing the characteristics of vertical pressure fluxes under those conditions. The estimated vertical pressure flux and its vertical variation are consistent with observations by other investigators (e.g., Bradshaw 1967; McBean and Elliott 1975; Högström 1990; Katul et al. 1996). Vertical pressure fluxes as functions of the separation distance between sonic anemometers and pressure sensors as well as atmosphere instability have been investigated by Burns et al. (2021).

For both tower and ABL data analyses, total air density is calculated using the ideal gas law with observed air temperature, water-vapor specific humidity, and pressure. To examine measurements during daytime, local standard time (LST) is used to relate meteorological measurements with the temporal variation of the surface heating/cooling impacted by the diurnal variation of solar radiation. To analyze measurements at night, coordinated universal time (UTC) is used for documenting an entire night within one calendar day to avoid confusion of specifying each night with two calendar days. At the CASES-99 site, LST is 6 h behind UTC. We only analyze Doppler lidar and radar observations for one calendar day at LAFO and GRAINEX; thus, LST is used for those observations.

3. Contribution of turbulent mixing to hydrostatic imbalance in the tower layer

Before we discuss contribution of turbulent mixing to the hydrostatic imbalance, we need to briefly discuss how turbulence is developed in the ABL, characteristics of turbulent mixing, and the role of large turbulent eddies in the vertical momentum balance.

a. Turbulence development in the atmospheric boundary layer

Turbulence is either generated by thermal forcing and/or by mechanical work of ambient flows and has significantly different characteristics in transferring a scalar depending on their generation mechanism, which was explained in Sun et al. (2016, 2020) and briefly summarized here for understanding contribution of turbulent mixing to hydrostatic imbalance. Turbulent motions represent airflows, which consist of molecule movement in organized direction different from random molecular motions associated with air temperature changes and is ubiquitous even in the calm stable boundary layer (SBL; e.g., Mahrt 2010, 2011, 2014). The thermally generated turbulent mixing under clear-sky conditions relies on the thermal energy source from surface diabatic heating. As the ground surface is heated by downward solar radiation, the heat transfer from the surface to the atmosphere is through molecular thermal diffusion in a thin air layer of $O(10^{-2}$ m), which is often referred as the surface laminar layer because of the limited distance that molecules travel and the negligibly small turbulent mixing adjacent to the surface (e.g., Foken 1978; Geiger et al. 1995; Sun et al. 1995; Vickers and Mahrt 2006). Associated with air warming, thermal expansion, which is not related to air incompressibility defined as air expansion/contraction under an invariant temperature, causes air density to decrease (more in section 3d). The resulting warmer and lighter air near the heating surface below the relatively colder and denser air above triggers positive buoyancy in generation of large and powerful turbulent eddies above the laminar layer leading to the development of the convective boundary layer (CBL). The vertical size of thermally generated turbulent eddies at a given distance above the surface, z, within the CASES-99 tower layer is found to approximately scale with z (e.g., Wyngaard 2010; Sun et al. 2016, 2020). Even with the help of mechanically generated turbulent eddies from strong wind shear, the warmer air is observed to remain near the surface and cannot be completely transferred into the ABL to achieve a neutral surface layer (yellow and dark blue temperature profiles in Fig. 1).

When the surface is cooled by longwave radiation at night, the cooled air from molecular thermal diffusion results in air contraction and air density increase near the surface in formation of the SBL. In contrast to thermally generated turbulent eddies, mechanically generated turbulent eddies from wind shear consume energy from environmental work for its generation of wind shear. Because the environmental mechanical work is independent of atmospheric stratification, wind shear–generated turbulent mixing under strong wind conditions can effectively mix the SBL toward a nearly neutral state while the production of the cold air from thermal diffusion at the surface is relatively slow. Sun et al. (2012, 2016, 2020) found that when wind speed V at a given height z above the surface is stronger than a threshold wind speed for the given location, the bulk wind shear V/z is effective in generating the most energetic large turbulent eddies that scale with z as well. When V at z is weaker than the threshold wind speed, the stable stratification as a result of the cold air from the cooling surface would reduce the vertical scale of the most energetic turbulent eddies, resulting in a weak turbulent mixing at z and the development of a relatively thin SBL. With the relatively warm residual layer from the daytime heating above the cold air layer developed at night, the air temperature

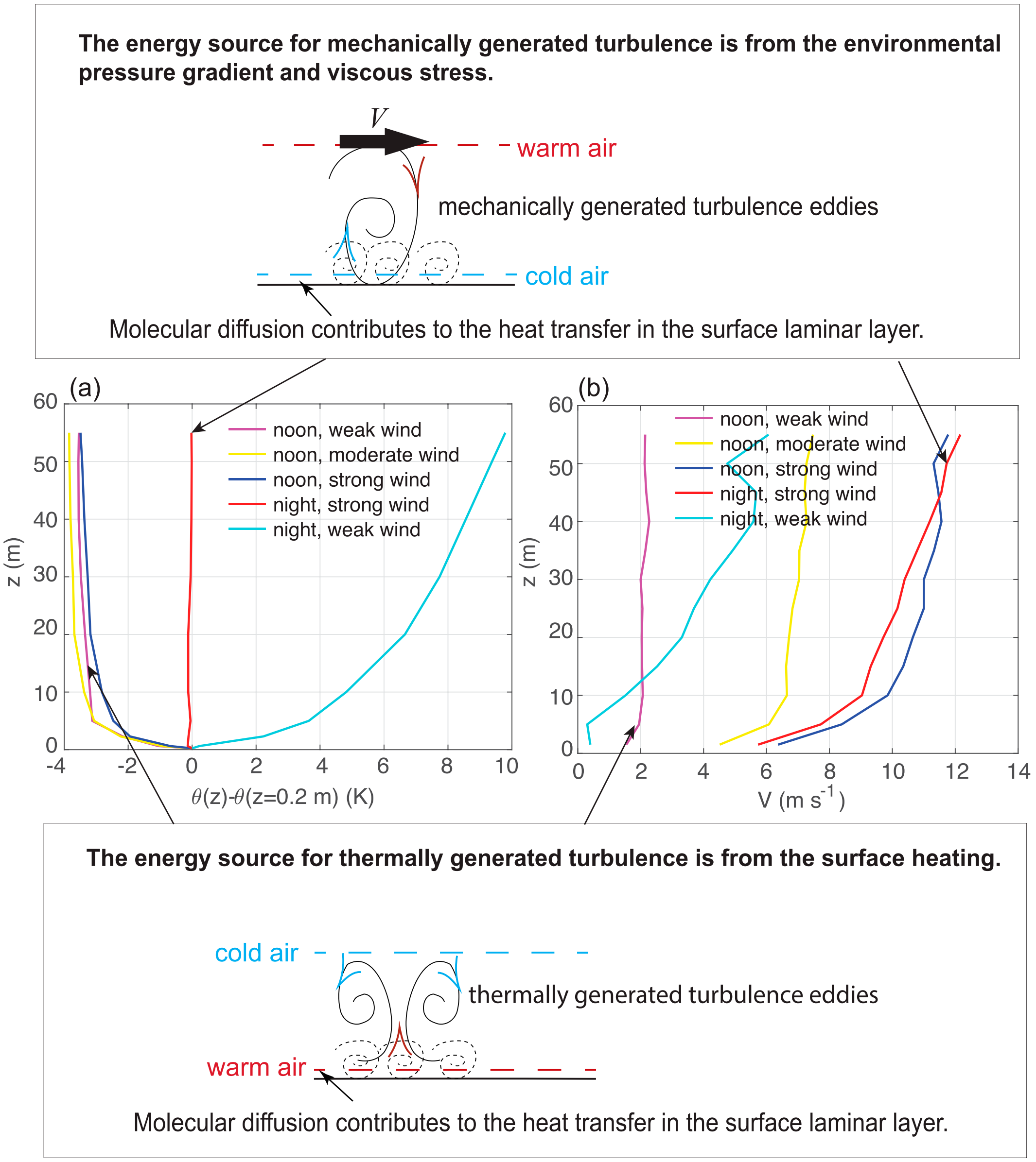

FIG. 1. (a) Potential temperature θ and (b) wind speed V profiles from the 60-m tower as a result of large-eddy turbulent mixing over a range of stability conditions: the free convective [noon, weak wind (10 Oct); magenta], convective [noon, moderate wind (14 Oct); yellow], weak convective [noon, strong wind (17 Oct); dark blue], neutral [night, strong wind (17 Oct); red], and very stable conditions [night, weak wind (10 Oct); cyan]. For easy comparison, the vertical variation of θ under the different stability conditions relative to its surface value at 0.2 m is plotted. Schematic illustrations of the mechanically generated turbulent mixing for the strong-wind night (red lines) and of thermally generated turbulent mixing for the free convective day (magenta lines) are sketched at the top and the bottom of the figure, respectively.

increases with height sharply at night (the cyan wind and temperature profiles in Fig. 1).

Overall, turbulence intensity reflects the strength of the energy source in turbulence generation. The vertical scale of the most energetic turbulent eddies in a horizontally homogeneous environment is determined by the vertical scale of the environment forcing in the stratified atmosphere, which is either bulk shear, which is the strongest wind shear at a given height, or the surface heating, which is determined by the air-surface temperature difference. The ability of turbulent eddies in transporting scalars is significantly different between thermally and mechanically generated turbulence as shown in Fig. 1.

b. *Characteristics of turbulent mixing*

The vertical turbulent transfer of a passive scalar ϕ is through the covariance between its turbulent perturbation ϕ'

and the vertical turbulent velocity perturbation w' integrated over an averaging scale $\overline{w'\phi'}$. Due to interactions between turbulent eddies, ϕ' at a given location varies constantly with time. As a result, the spatial variation of ϕ', for example, $\partial\phi'/\partial z$, would vary significantly in space and time depending on the vertical variation of ϕ', $\delta\phi'$, over the distance of δz used for estimating $\partial\phi'/\partial z$. In contrast, $\overline{w'\phi'}$ is consistent with the vertical gradient $\overline{\phi}$ on a scale larger than the vertical scale of the most energetic eddies. If $\overline{\phi}$ increases with height, the upward branch of turbulent eddies would bring smaller ϕ upward, that is, $w' > 0$ and $\phi' < 0$; the downward branch of turbulent eddies would bring larger ϕ downward, that is, $w' < 0$ and $\phi' > 0$. In either situation, $\overline{w'\phi'}$ would be steadily negative. To capture a statistical meaningful $\overline{w'\phi'}$, the averaging scale needs to be large enough to capture many of the most energetic turbulent eddies. Because the Reynolds-averaged ϕ, $\overline{\phi}$, is controlled by its vertical transfer, $\overline{w'\phi'}$, under horizontally homogeneous conditions, a steady vertical variation of $\overline{w'\phi'}$ would result in a steady vertical variation of $\overline{\phi}$.

c. *The role of large turbulent eddies in the vertical momentum balance*

The net vertical transfer of ϕ consists of its vertical turbulent transport, $\overline{w'\phi'}$, as well as its transport by the Reynolds averaged mean vertical motion, $\overline{w}\overline{\phi}$. The latter is often investigated in nonhydrostatic models with assumed small contribution from the turbulent transfer (e.g., Cotton et al. 2010). Because synoptic vertical motions are much smaller than vigorous up and down motions of large turbulent eddies in the ABL and the Reynolds averaged w over many of those up and down large turbulent eddies constrained by the fluid continuity equation is negligibly small as well, thus, $\overline{w} \approx 0$ (more in sections 3d and 4a). Therefore, the vertical momentum balance equation, Eq. (2), can be further simplified as

$$\overline{\rho}\frac{\partial\overline{w'^2}}{\partial z} \approx -\left(\frac{\partial\overline{p}}{\partial z} + \overline{\rho}g\right) + \frac{\mu}{\overline{\rho}}\overline{\rho'\frac{\partial^2 w'}{\partial z^2}}. \tag{3}$$

Equation (3) indicates that the acceleration of the most energetic large nonlocal turbulent vertical velocity can be dominated by the vertical variation of the most energetic large nonlocal turbulent vertical velocity variance, $\partial\overline{w'^2}/\partial z$, and is driven by $-(1/\overline{\rho})(\partial\overline{p}/\partial z + \overline{\rho}g)$, which is determined by the balance between the positive mean vertical pressure-gradient force $-\partial\overline{p}/\partial z$, as $\partial\overline{p}/\partial z$ is normally negative, and the negative mean gravity force $-\overline{\rho}g$ as the mean air density $\overline{\rho}$ is always positive. The viscous force [the last term in Eq. (3)] in reducing momentum through air viscosity and molecule collisions with different speeds depends on spatial variations of vertical turbulent motions and can be strong near the surface due to air–land interactions. Governed by the ideal gas law, the mechanical force of hydrostatic imbalance can be strongly impacted by atmospheric thermodynamics as well. Because $\overline{w'^2}$ is a component of turbulent kinetic energy, the temporal variation of $\overline{w'^2}$, $\partial\overline{w'^2}/\partial t$, is governed by the kinetic energy balance; however, its vertical variation, $\partial\overline{w'^2}/\partial z$, is controlled by the vertical momentum balance, which is dominated by the hydrostatic imbalance.

d. *Contribution of turbulent transfer of air mass to hydrostatic imbalance*

Vertical turbulent mixing can effectively transport air density, resulting in vertical variations of pressure and air density and contribute to the hydrostatic imbalance. We examine the relationship between observed $\partial\overline{w'^2}/\partial z$ and $-(1/\overline{\rho})(\partial\overline{p}/\partial z + \overline{\rho}g)$ within the CASES-99 tower layer under a range of atmospheric stratification conditions associated with varying surface diabatic heating/cooling and wind speeds knowing different characteristics of thermally and mechanically generated turbulence in turbulent heat transfer from section 3a. These include a nearly free convective day on 10 October, which is characterized with steady weak wind on a clear convective day (left column, Fig. 2); a convective day with moderate winds on 14 October (right column, Fig. 2); a nearly neutral night with strong winds during the night of 16 October and the early morning of 17 October (the UTC night of 17 October, left column in Fig. 3); and a very stable night with weak winds during the night of 9 October and the early morning of 10 October (the UTC night of 10 October, right column in Fig. 3). The vertical wind and temperature profiles for the four cases are shown in Fig. 1.

We find that $\overline{w'^2}$ increases with z in all four cases (Fig. 4), implying that the atmospheric mean state is hydrostatically imbalanced with $-(1/\overline{\rho})(\partial\overline{p}/\partial z + \overline{\rho}g) > 0$ under all the stability conditions [Eq. (3)]. To directly estimate $-(1/\overline{\rho})(\partial\overline{p}/\partial z + \overline{\rho}g)$, we use $\overline{\rho}$ averaged between 1.5 and 30 m. The direct estimates of $-\partial\overline{p}/\partial z$ and $\overline{\rho}g$ indicate that the positive force $-\partial\overline{p}/\partial z$ is indeed larger than the negative force $-\overline{\rho}g$ for all the four cases, suggesting that $-(1/\overline{\rho})(\partial\overline{p}/\partial z + \overline{\rho}g) > 0$ contributes to the observed $\partial\overline{w'^2}/\partial z > 0$ within the lower tower layer.

To examine how the hydrostatic imbalance is developed, we first study contribution of thermal expansion/contraction on the relationship among air density, temperature, and pressure. According to the ideal gas law and the definition of potential temperature θ, perturbations of p, ρ, and θ, expressed as δp, $\delta\rho$, and $\delta\theta$, are related as $(c_v/c_p)\delta p/\overline{p} = \delta\rho/\overline{\rho} + \delta\theta/\overline{\theta}$, where c_v and c_p are the specific heat at constant volume and pressure, respectively. That is, any air temperature change would impact not only air density but also air pressure changes. Based on the observed standard deviation of p, $\sigma_p \approx 2$ Pa, and the observed standard deviation of θ, $\sigma_\theta \approx 1$ K at either 0.5 or 1.5 m during the entire CASES-99, $\sigma_\theta/\overline{\theta} \approx 1/300 \approx O(10^{-3})$ is much larger than $\sigma_p/\overline{p} \approx 0.02/1000 \approx O(10^{-5})$, implying that $\delta\rho/\overline{\rho} \approx -\delta\theta/\overline{\theta}$. That is, thermal expansion/contraction dominates the relationship between air density and temperature during the entire CASES-99—an air density increase/decrease is closely related to an air temperature decrease/increase as a result of thermal contraction/expansion. The close negative correlation between air temperature and density also suggests that $(c_v/c_p)\delta p/\overline{p}$ is a small difference between $\delta\rho/\overline{\rho}$ and $\delta\theta/\overline{\theta}$. The observed relatively small variation of p is consistent with early studies of the Boussinesq approximation (e.g., Mahrt 1986; Schlichting and Gersten 2000).

Associated with the air temperature increase on the free convective day, the air pressure is observed to decrease from its large-scale increasing trend (Fig. 6a) indicating that the

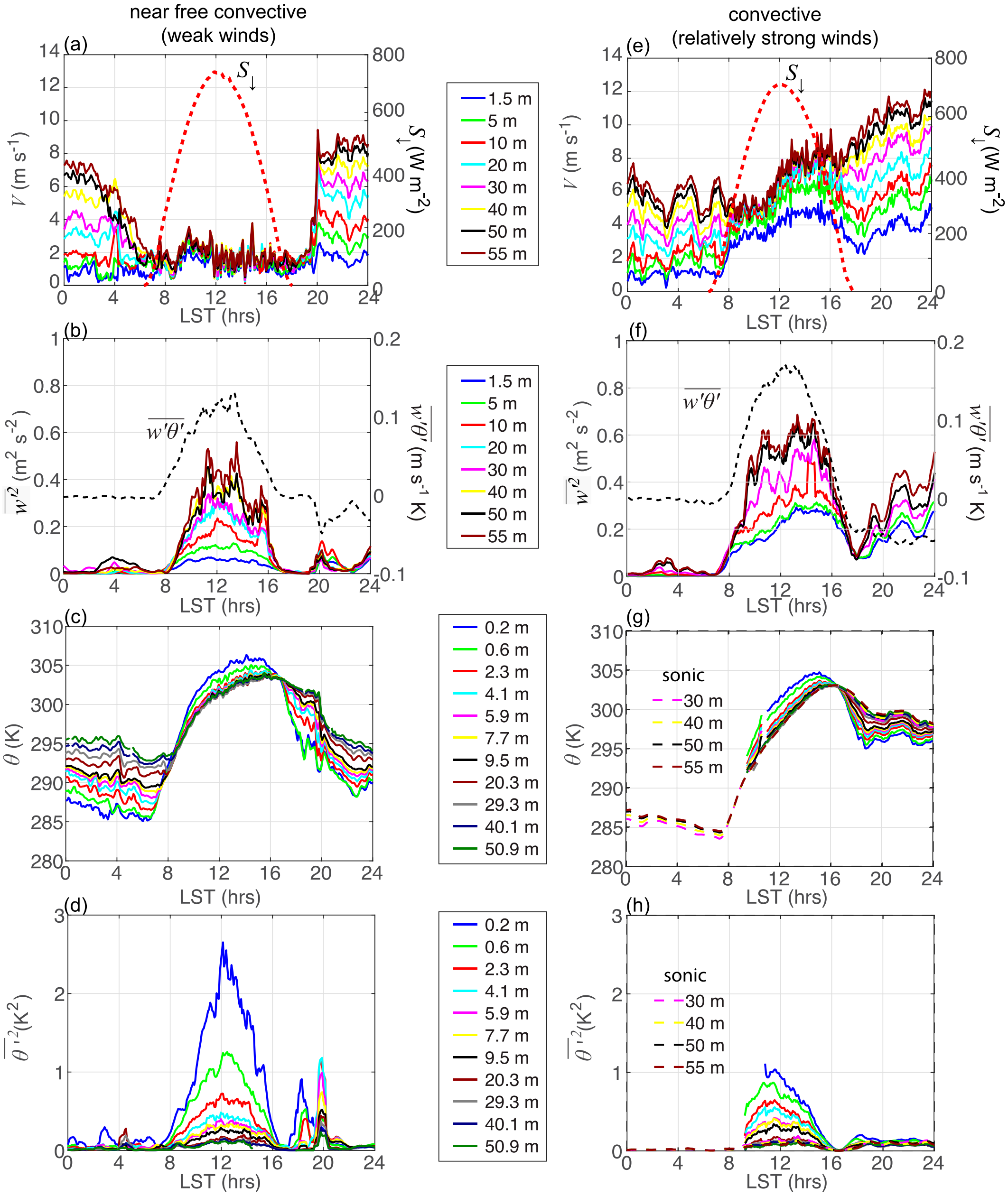

FIG. 2. (a),(e) Observed temporal variations of downward solar radiation $S_\downarrow$ and wind speed V; (b),(f) vertical velocity variances $\overline{w'^2}$ and kinematic heat flux $\overline{w'\theta'}$ at 1.5 m (the black dashed line); (c),(g) potential temperatures θ; and (d),(h) the variance of potential temperature $\overline{\theta'^2}$ at the labeled heights for (left) the free convective day 10 Oct and (right) the moderate convective day 14 Oct. The plots in (c), (d), (g), and (h) are from the thermocouples. Because of the thermocouple instrument issue on the morning of 14 Oct, the sonic temperature measurements from 30 m and up (dashed curves) are added in (g) and (h) to show the diurnal variations of θ and $\overline{\theta'^2}$ on the day. An hourly running mean of the 5-min dataset is used for all of the plots. The wind and potential temperature profiles at noon for these two cases are shown in Fig. 1.

pressure decrease is dominated by the air density decrease based on the ideal gas law. The relationship among air density, temperature, and pressure can be further examined through their vertical fluxes following the ideal gas law, $(c_v/c_p)\overline{w'p'}/\overline{p} = \overline{w'\rho'}/\overline{\rho} + \overline{w'\theta'}/\overline{\theta}$. The close negative correlation between ρ decrease and θ increase is indeed observed in the close relationship between $-\overline{w'\rho'}$ and $(\overline{\rho}/\overline{\theta})\overline{w'\theta'}$ in Fig. 5b. The dominance of air density on air pressure is also observed in the negative $\overline{w'p'}$ at both 1.5 and 30 m (Fig. 5c). The observed increasing magnitude of the negative $\overline{w'p'}$ with height, that is, $\partial\overline{w'p'}/\partial z < 0$, is due to the enhanced $|w'|$ and $|p'|$ at 30 m transported by the most energetic turbulent eddies with

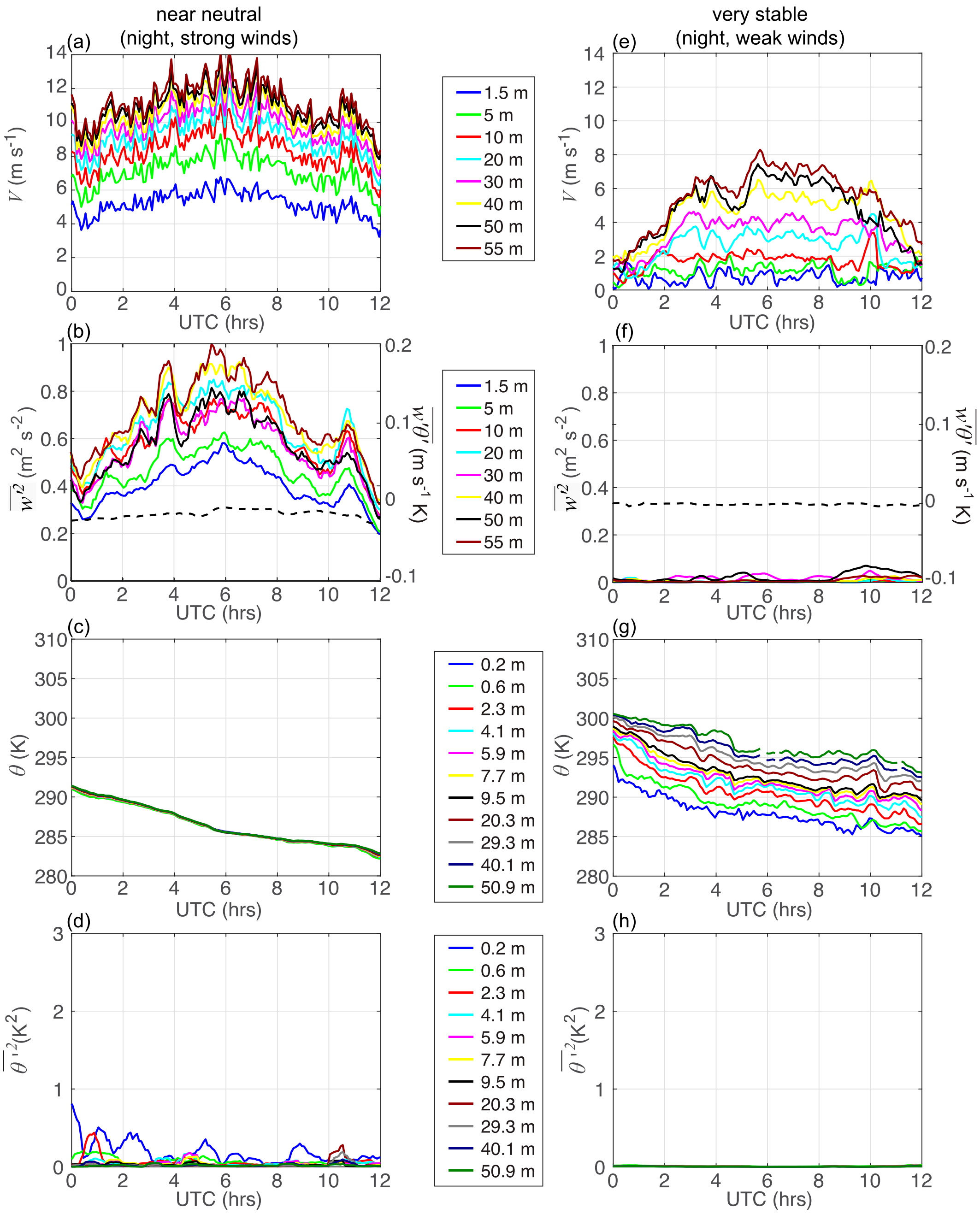

FIG. 3. As in Fig. 2, but for two nights when $S_\downarrow = 0$: (left) the UTC night of 17 Oct (approximately from sunset on 16 Oct to sunrise on 17 Oct), which represents a nearly neutral condition with strong winds, and (right) the UTC night of 10 Oct (approximately from sunset on 9 Oct to sunrise on 10 Oct), which represents a very stable condition with weak winds. The wind and potential temperature profiles for these two cases are shown in Fig. 1.

the increasing vertical scale from the surface into the ABL (section 3a). The seemingly countergradient pressure flux against the vertical decrease of p here is because pressure is not a passive scalar and is strongly influenced by the air density change associated with the air temperature change.

We then investigate how vertical turbulent transfers of air density and pressure on the free convective day contribute to the vertical variations of $\overline{\rho}$ and $\overline{p}$, which in turn enhance the hydrostatic imbalance of the mean state. When the surface temperature T_s from downward solar radiation $S_\downarrow$ is larger than the surface air temperature at 0.2 m, T_a, that is, $T_s - T_a > 0$ (Fig. 5a), air density is reduced as a result of air thermal expansion (Fig. 4a). As the distance from the surface increases, the impact of the surface heating on thermally generated turbulence

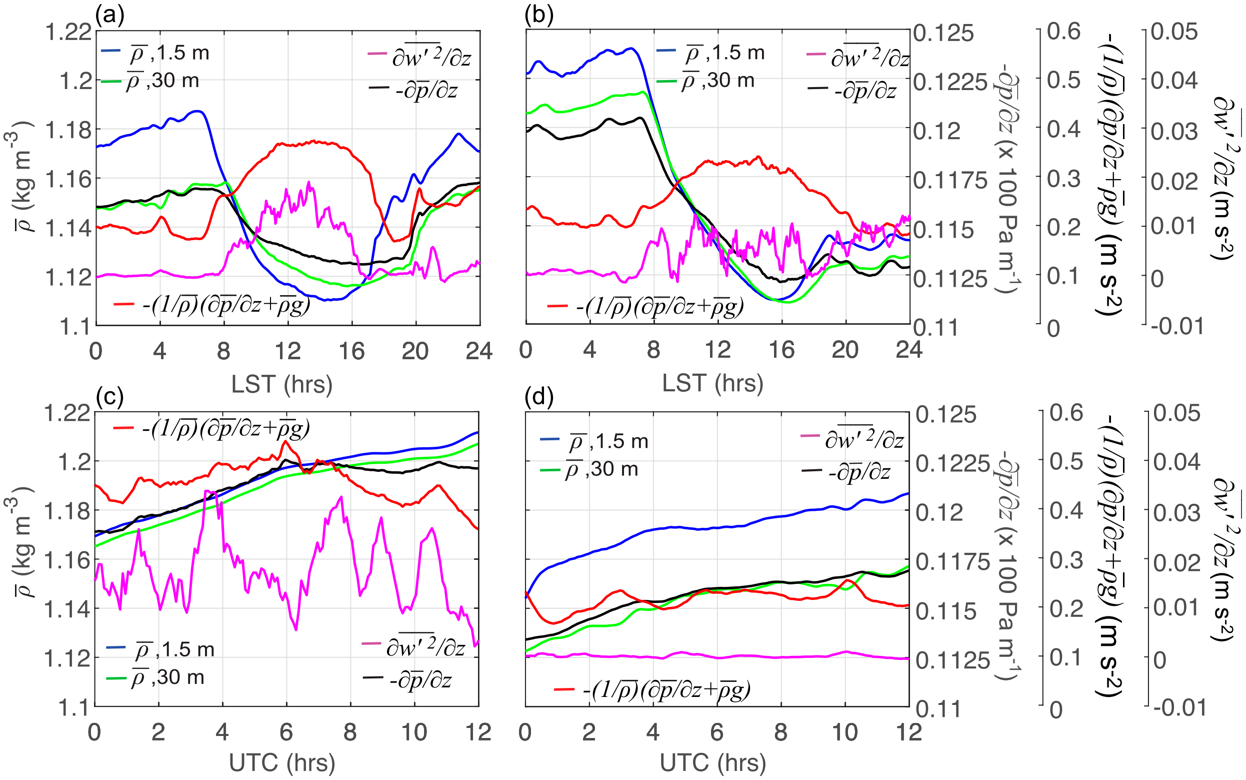

FIG. 4. Air density $\overline{\rho}$ at 1.5 and 30 m; the vertical pressure-gradient force $-\partial\overline{p}/\partial z$ estimated using $\overline{p}$ between 1.5 and 30 m; the vertical gradient of $\overline{w'^2}$ between 1.5 and 5 m, i.e., $\partial\overline{w'^2}/\partial z$; and the corresponding hydrostatic imbalance $-(1/\overline{\rho})(\partial\overline{p}/\partial z + \overline{\rho}g)$ in Eq. (3) on (a) the free convective day 10 Oct, (b) the convective day with moderate winds 14 Oct, (c) the nearly neutral night with strong winds on the UTC night of 17 Oct, and (d) the very stable night with weak winds on the UTC night of 10 Oct. Note that LST is used for the daytime cases (a) and (b) and UTC is used for the nighttime cases (c) and (d) so that each night is within the same calendar day. The averaged $\overline{\rho}$ between 1.5 and 30 m is used in the calculated hydrostatic imbalance.

decreases, resulting in the decreasing air temperature (Fig. 2c), the decreasing temperature variance, $\overline{\theta'^2}$ (Fig. 2d), and the decreasing air density reduction with height (Fig. 4a). Consequently, the air density is observed to be less at 1.5 m than at 30 m for the convective period in Fig. 4a, leading to positive buoyancy, upward heat flux, $\overline{w'\theta'} > 0$, and downward air density flux, that is, upward transfer of relatively low-density air, $\overline{w'\rho'} < 0$ (Fig. 5b). Similar to the vertical decrease of the air density reduction, the air pressure decrease is observed to be more near the surface than above as well (Figs. 6a,c). That is, the upward transport of the warm and low-density air reduces the positive value of $-\partial\overline{p}/\partial z$ (or less negative $\partial\overline{p}/\partial z$). Because of the relatively small change of air pressure in response to the air temperature change, the reduction of the positive value of $-\partial\overline{p}/\partial z$ is less than the reduction of the air density. With the large background $-\partial\overline{p}/\partial z$, $(\partial\overline{p}/\partial z + \overline{\rho}g)$ becomes increasingly positive under convective conditions and is responsible for the increasingly positive $\partial\overline{w'^2}/\partial z$ with the surface heating (Fig. 4a). The observed close connection between $\partial\overline{w'^2}/\partial z$ and $-(1/\overline{\rho})(\partial\overline{p}/\partial z + \overline{\rho}g)$ indicates that the so-called positive buoyancy for the vertical turbulence enhancement from the surface heating as shown in $\partial\overline{w'^2}/\partial z > 0$ is essentially achieved by the enhanced hydrostatic imbalance, which is dominated by the reduction of the negative gravity force from the upward transfer of low-density air.

After $S_\downarrow$ starts to decrease in the afternoon, the thermal energy source for generating turbulence decreases following the $T_s - T_a$ reduction (Fig. 5). The consistency between $T_s - T_a$ and the upward heat flux $\overline{w'\theta'}$ indicates that the CBL remains as long as $T_s - T_a > 0$ but the instability decreases with decreasing $T_s - T_a$ (Figs. 5a,b). Thus, both $-\partial\overline{p}/\partial z$ (negative $\partial\overline{p}/\partial z$) and $\overline{\rho}$ reach to their daily minimum in the afternoon; however, the resulting $-(1/\overline{\rho})(\partial\overline{p}/\partial z + \overline{\rho}g) > 0$ is observed to reach to its maximum around noon so does $\partial\overline{w'^2}/\partial z$ (Fig. 4a).

With the moderate wind speed on the convective day of 14 October (Fig. 2), the contribution of mechanically generated turbulence helps lifting the relatively warm and low-density air near the surface upward, leading to the larger heat flux $\overline{w'\theta'}$, the larger temporal reduction of $\overline{\rho}$ and $-\partial\overline{p}/\partial z$, and the reduced vertical air density difference in comparison with the free convective day (Figs. 4a,b). Consequently, both $-(1/\overline{\rho})(\partial\overline{p}/\partial z + \overline{\rho}g)$ and $\partial\overline{w'^2}/\partial z$ are consistently smaller on the moderate wind convective day. The daytime reduction of both $-\partial\overline{p}/\partial z$ (less negative) and $\overline{\rho}$ as well as the daytime increase of $\partial\overline{w'^2}/\partial z$ are evident throughout the entire CASES-99 (Fig. 7).

At night, mechanically generated turbulent mixing lifts the cold and dense air from the surface upward, increasing $\overline{\rho}$, $\overline{p}$, and $-\partial\overline{p}/\partial z$ especially when wind speeds are strong such as

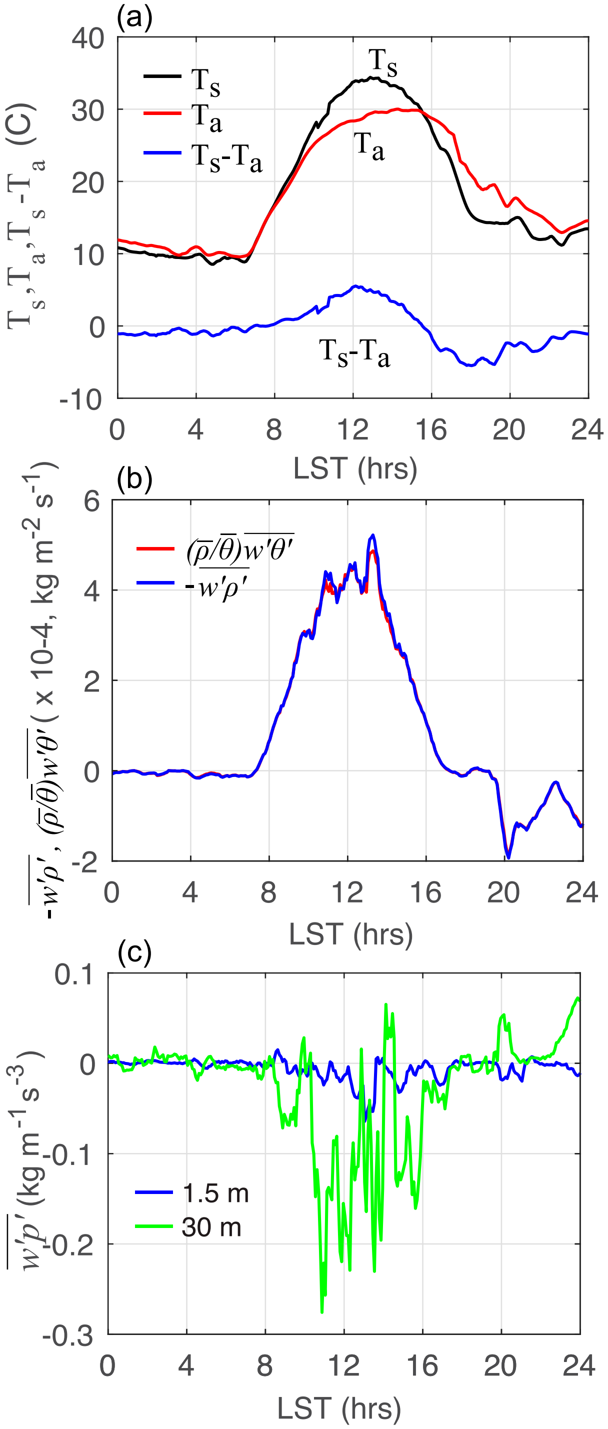

FIG. 5. (a) The surface radiation temperature T_s, the air temperature at 0.2 m T_a, and the difference between the two; (b) a comparison between the negative air density flux $-\overline{w'\rho'}$ and the positive heat flux scaled according to the ideal gas law $(\overline{\rho}/\overline{\theta})\overline{w'\theta'}$ measured at 1.5 m; and (c) vertical pressure fluxes $\overline{w'p'}$ at 1.5 and 30 m on 10 Oct.

the UTC night of 17 October (Figs. 3, 4c, and 6b,c). Because $-\partial\overline{p}/\partial z$ is enhanced more than $\overline{\rho}g$ (Fig. 4c), the increasing $-(1/\overline{\rho})(\partial\overline{p}/\partial z + \overline{\rho}g) > 0$ with wind speed is observed in support of the increasing $\partial\overline{w'^2}/\partial z$ at this weakly stable night. Contribution of the mechanically generated turbulent mixing to $-\partial\overline{p}/\partial z$ in response to the wind speed increase and decrease before and after 0600 UTC (Fig. 3b) evince in Fig. 4c. Under weak wind conditions without influence of significant gravity waves to enhance turbulence intensity (e.g., Sun et al. 2015) during the UTC night of 10 October, the weak vertical turbulent mixing as shown in small $\overline{w'^2}$ and $\overline{\theta'^2}$ (Figs. 3f,h) could not visibly impact the strong stable stratification (Fig. 3g). Thus, the hydrostatic imbalance is not significantly impacted by the weak turbulent mixing in the SBL (Fig. 4d).

Overall, the hydrostatic imbalance is observed within the tower layer throughout CASES-99. The hydrostatic imbalance is the consequence of thermal expansion/contraction in changing air density following air temperature changes through both molecular diffusion in the surface laminar layer and turbulent mixing above. Turbulent mixing in response to the diurnal variation of the surface diabatic heating/cooling and wind shear causes the vertical transport of lighter/heavier air upward resulting in the diurnal oscillations of $-\partial\overline{p}/\partial z$, $\overline{\rho}$, and $-(\partial\overline{p}/\partial z + \overline{\rho}g)$. Because of the relatively large vertical pressure gradient near the surface despite the vertical turbulent transport of different air mass, $-(\partial\overline{p}/\partial z + \overline{\rho}g)$ remains positive in the lower ABL as evident in the observed $\partial\overline{w'^2}/\partial z > 0$ (Fig. 7). The importance of the vertical pressure gradient in the vertical momentum balance was also concluded, for example, by Kaimal and Businger (1970) in their observational analyses of thermal plumes and dust devils. Among the four cases that range from the most convective, the most neutral, to the most stable cases during CASES-99, we find that the largest $(\partial\overline{p}/\partial z + \overline{\rho}g)$ occurred at the strong-wind night and the smallest imbalance occurred at the very stable night. Because mechanically generated turbulent mixing consumes environmental work through wind shear and can effectively transfer heat. In contrast, thermally generated turbulent mixing relies on positive buoyancy from heat transfer (section 3a). Therefore, the corresponding hydrostatic imbalance of the mean state can be larger in the night under the strong wind than the free convective day. Because $\partial\overline{w}/\partial t$ is an order of magnitude smaller than $\partial\overline{w'^2}/\partial z$ in the tower layer, the observed relatively large $-(1/\overline{\rho})(\partial\overline{p}/\partial z + \overline{\rho}g)$ in comparison with $\partial\overline{w'^2}/\partial z$ in Fig. 4 suggests possible important contributions of air–land interactions to momentum dissipation in Eq. (3).

4. Hydrostatic imbalance in the atmospheric boundary layer

Knowing $\partial\overline{w'^2}/\partial z$ is well correlated with the hydrostatic imbalance of the mean state in the bottom layer of the atmosphere, we examine how $\partial\overline{w'^2}/\partial z$ varies in the entire ABL, and whether it is a good indicator for the hydrostatic imbalance in the ABL as well.

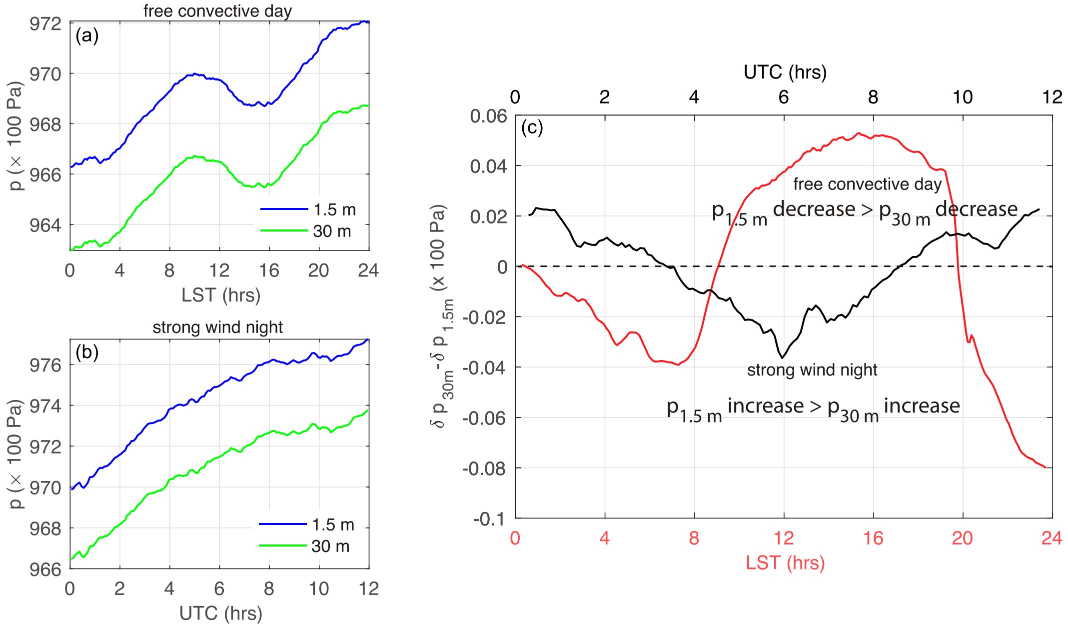

FIG. 6. The air pressure p at 1.5 and 30 m (a) on the free convective day 10 Oct in LST and (b) at the strong-wind UTC night of 17 Oct. Also shown is (c) the vertical difference of the pressure daily variation δp between 30 and 1.5 m, $\delta p_{30\mathrm{m}} - \delta p_{1.5\mathrm{m}}$, during the free convective day (red curve and abscissa) and the strong-wind night (black curve and abscissa above the plot). The pressure daily variation δp at each level is obtained by linear detrending of the observed pressure. Because pressure decreases at both 1.5 and 30 m during the free convective day, the positive value of the red $\delta p_{30\mathrm{m}} - \delta p_{1.5\mathrm{m}}$ curve in (c) indicates that the pressure decrease is more at 1.5 m than at 30 m. At night, pressure increases at both levels and the negative value of the black $\delta p_{30\mathrm{m}} - \delta p_{1.5\mathrm{m}}$ curve in (c) implies that the pressure increase is more at 1.5 m than at 30 m.

a. *Vertical variations of vertical velocity variances*

Using the Doppler lidar data described in section 2b, the vertical and horizontal turbulent motions in response to the surface heating/cooling are investigated for a relatively weak wind and clear-sky day, 23 August 2022 (Fig. 8). We concentrate on the lidar data within 2 km above the surface where the air layer is strongly impacted by the surface diurnal heating/cooling and the lidar signal is strong. In the early morning before sunrise, the SBL is developed due to a weak surface wind over the radiatively cool surface (Fig. 8a). Because the stable stratification reduces interactions between the atmosphere and the surface, a low-level jet (LLJ) establishes above the SBL (Fig. 8c), which is commonly observed (e.g., Banta et al. 2002, 2007; Li et al. 2018). Following the gradual increase of the surface temperature after sunrise (Fig. 8a), turbulent intensity increases gradually during 0700–1100 LST and becomes strong during the most convective period of 1100–1700 LST as shown in strong up and down large-eddy turbulent vertical motions (Fig. 8b). Constrained by flow continuity, horizontal wind is observed to oscillate from the airflow convergence/divergence in response to strong up and down large vertical turbulent motions (Fig. 8c). The observed temporal variation of wind direction reflects the upward vertical turbulent motion in bringing up the southerly surface wind and the downward vertical motion in bringing down the northerly wind (Fig. 8d). The intensity of the turbulent vertical motion in the CBL is reduced in the afternoon until sunset following the decrease of the surface temperature due to the reduction of downward solar radiation. After about 1700 LST, the surface becomes a heat sink to the atmosphere, turbulent mixing in the entire ABL decreases, and an LLJ above the SBL appears again.

We then calculate the standard deviation of w, σ_w, to capture turbulence variation as a function of height over the entire ABL and the entire day of 23 August (Fig. 9). To investigate the impact of the diurnal variation of the surface heating/cooling on turbulence strength, we divide the entire day into four time periods as shown in Fig. 8: the nighttime period between midnight to sunrise, the early-morning CBL development period, the vigorous convective period, and the after-sunset SBL period. To understand the temporal and vertical development of the size of turbulent eddies, we first examine the variation of σ_w with the size of data segments from 5 to 120 min as a function of height for the four periods (Fig. 9). To ensure the sampling size especially for large data segments at each height, we calculate σ_w with the running window for each segment by shifting the segment window one data point at a time, which is 10 s, along the w time series at each height. The value of σ_w for each segment size at each height is then obtained by averaging all the σ_w values from the running window of the segment at the height.

The observed variation of σ_w with the size of the data segments, local time periods, and height demonstrates the dependence of the size of the most energetic turbulent eddies on turbulence generation mechanism and the distance away from

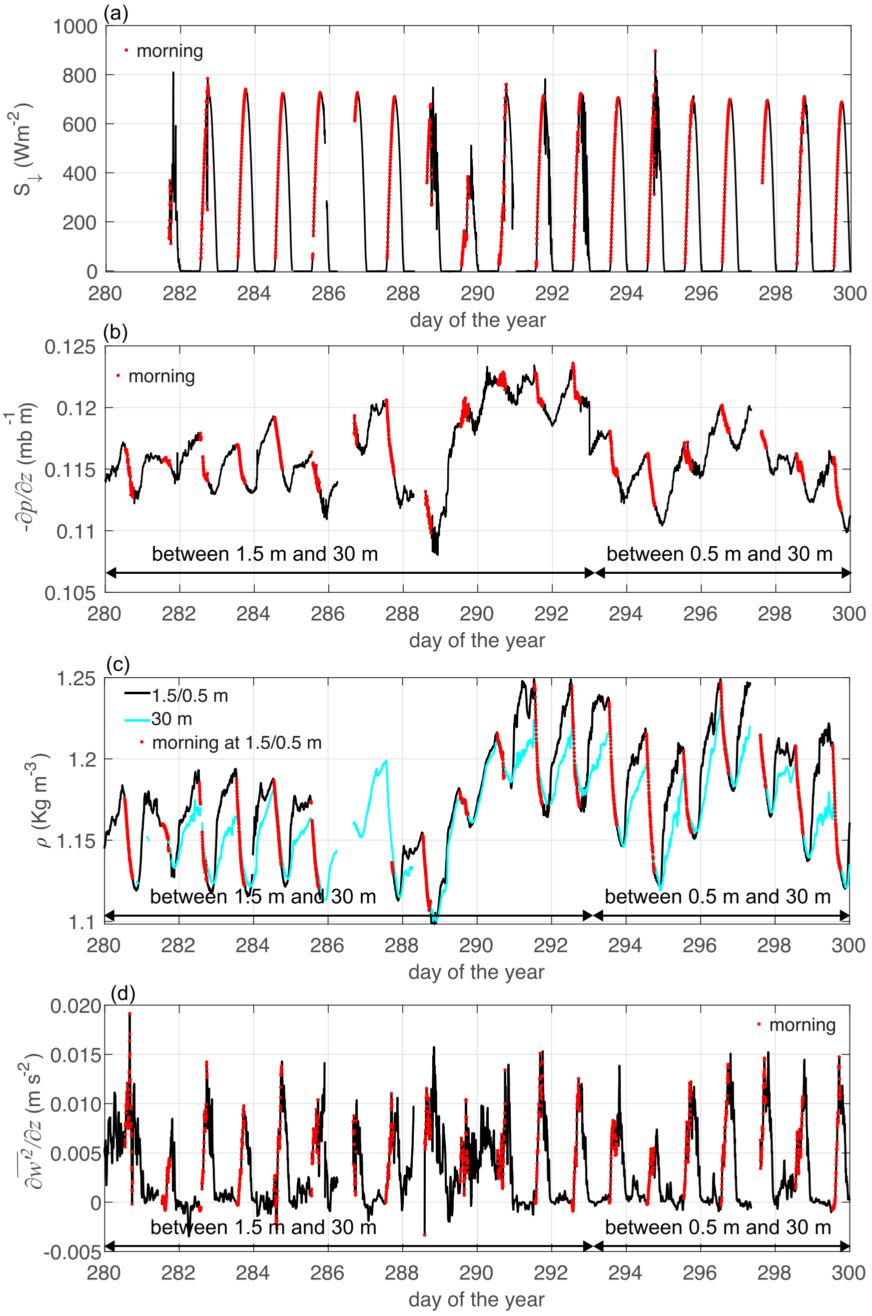

FIG. 7. Observed diurnal variations of (a) downward solar radiation $S_\downarrow$, (b) vertical pressure gradient $-\partial p/\partial z$ between 1.5/0.5 m (see section 2 for the data description) and 30 m, (c) air density ρ at 1.5/0.5 and 30 m, and (d) $\partial \overline{w'^2}/\partial z$ between 1.5/0.5 and 30 m during the entire CASES-99. The morning observations are marked in red for easy detection of the $-\partial p/\partial z$ decrease (i.e., the $\partial p/\partial z$ increase) and the ρ decrease responsible for the hydrostatic imbalance as well as the $\partial \overline{w'^2}/\partial z$ increase following the $S_\downarrow$ increase. The pressure sensor as well as the sonic anemometer at the lowest level were moved from 1.5 to 0.5 m on day 293 (20 Oct); the two time periods were marked in (b)–(d). The days here are in UTC.

the surface (Fig. 9). The observed decrease of σ_w toward the surface for all the data segments and their convergence to the 5-min σ_w regardless of the turbulence generation mechanisms either thermally or mechanically indicate the impact of the surface drag on diminishing the size and strength of turbulent eddies. The observed increase of σ_w with the size of the data segment at a given height and the vertical increase of σ_w with height for a given data segment demonstrate the growth of

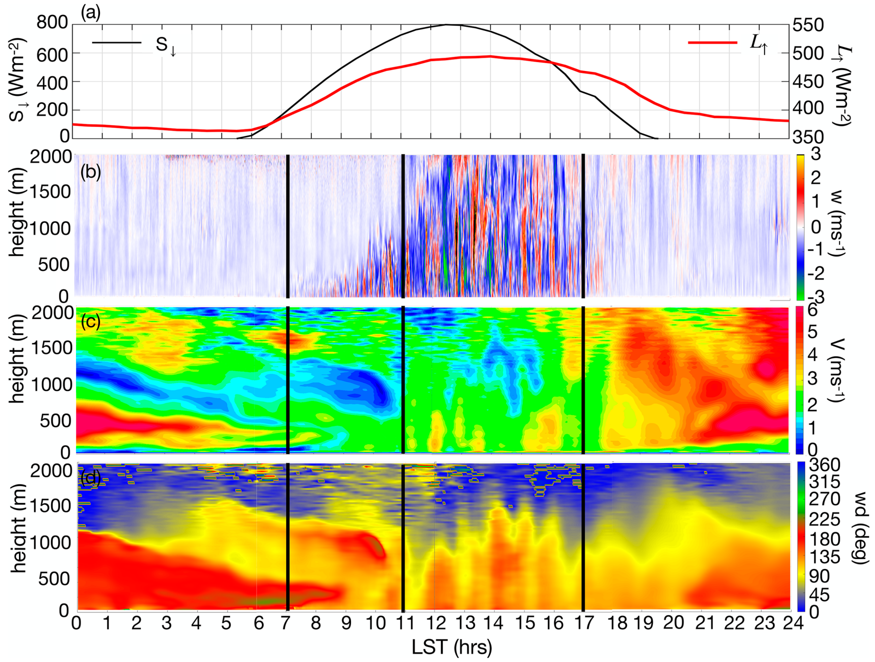

FIG. 8. (a) The downward solar radiation $S_\downarrow$ and the upward longwave radiation $L_\uparrow$, and (b) the vertical velocity w, (c) the horizontal wind speed V, and (d) the horizontal wind direction (wd) as functions of height above the surface, all during the free convective day of 23 Aug 2022. The vertical black lines mark the time periods of the early-morning stable period, the morning CBL development, the deep convective period, and the evening period used for Figs. 9 and 10, described below. Here we only concentrate on the observations from the surface up to about 2000 m where the diurnal variation of the signals is strong.

turbulent eddies with height. Evidently, the fastest growth of σ_w with height occurs during the most convective period of 1100–1700 LST (Fig. 9a), suggesting contribution of the surface heating to the growth of turbulent eddies. During this period, σ_w reaches to its maximum value from the 5-min data segment near the surface to about 90-min at ~500 m where the daily maximum σ_w is achieved. Further increasing the segment size does not contribute significantly to σ_w at each height. This observation demonstrates that the size of the most energetic turbulent eddies generated by the surface heating increases with height and these most energetic eddies dominate turbulence intensity, which is consistent with the tower data analysis in Sun et al. (2016, 2020) and the numerical investigation by Zhou et al. (2019). The impact of the surface heating on the growth of the size of the most energetic eddies is also evident in the growth of the vertical maximum σ_w from 0.65 m s^{-1} at ~150 m during 0700–1100 LST to 1.4 m s^{-1} at ~500 m during 1100–1700 LST. As the heat flux transfer is reduced with increasing distance from the heating surface, the size of the most energetic turbulent eddies above the height of the maximum σ_w decreases with height.

After sunset, the thermal impact of the surface to the atmosphere is reversed from being the thermal source to the thermal sink. Due to the lack of strong mechanically generated turbulence and the impact of the surface drag and air viscosity on reducing turbulence intensity, the size of the most energetic turbulent eddies that contributes to σ_w in the entire daytime CBL is significantly reduced at night (Fig. 9d). Consequently, σ_w approaches to its early-morning value before sunrise (Figs. 9b,d). The similar nonmonotonical vertical variation of σ_w at night and above the height of the largest σ_w in the upper CBL in contrast to the relatively smooth vertical increase of σ_w in the lower CBL reveals the characteristic difference between the intermittent turbulence decay regime and the relatively homogenous active turbulence generation regime in the lower CBL.

Similar vertical variations of $\overline{w'^2}$ have also been observed in the ABL with various atmospheric stratifications in the literature. Lenschow et al. (1980) observed that $\overline{w'^2}$ increased with height up to about 0.3 z_i and decreased from 0.3 z_i up to z_i in the CBL, where z_i is the CBL height and ranges between 680 to 1900 m (their Fig. 4). The decreasing $\overline{w'^2}$ with height at the upper CBL was also observed by Lenschow et al. (2012, 2000). Similar vertical variations of $\overline{w'^2}$ were observed with sonic anemometers up to 132 m over a coastal zone (Acevedo et al. 2018), with lidar observations in the air layer below 2 km at night (Bonin et al. 2020), below 1 km after the passage of a squall line during daytime (Bezerra et al. 2021), and within clouds (Wang and Geerts 2013). Similar to the surface diabatic heating, water condensation also releases heat. The vertical variation of $\overline{w'^2}$ was clearly observed during cloud formation where latent heat release is expected to be large (e.g., Atlas et al. 2020). Over the North Atlantic where the surface diurnal variation is weak, Shaw and Businger (1985)

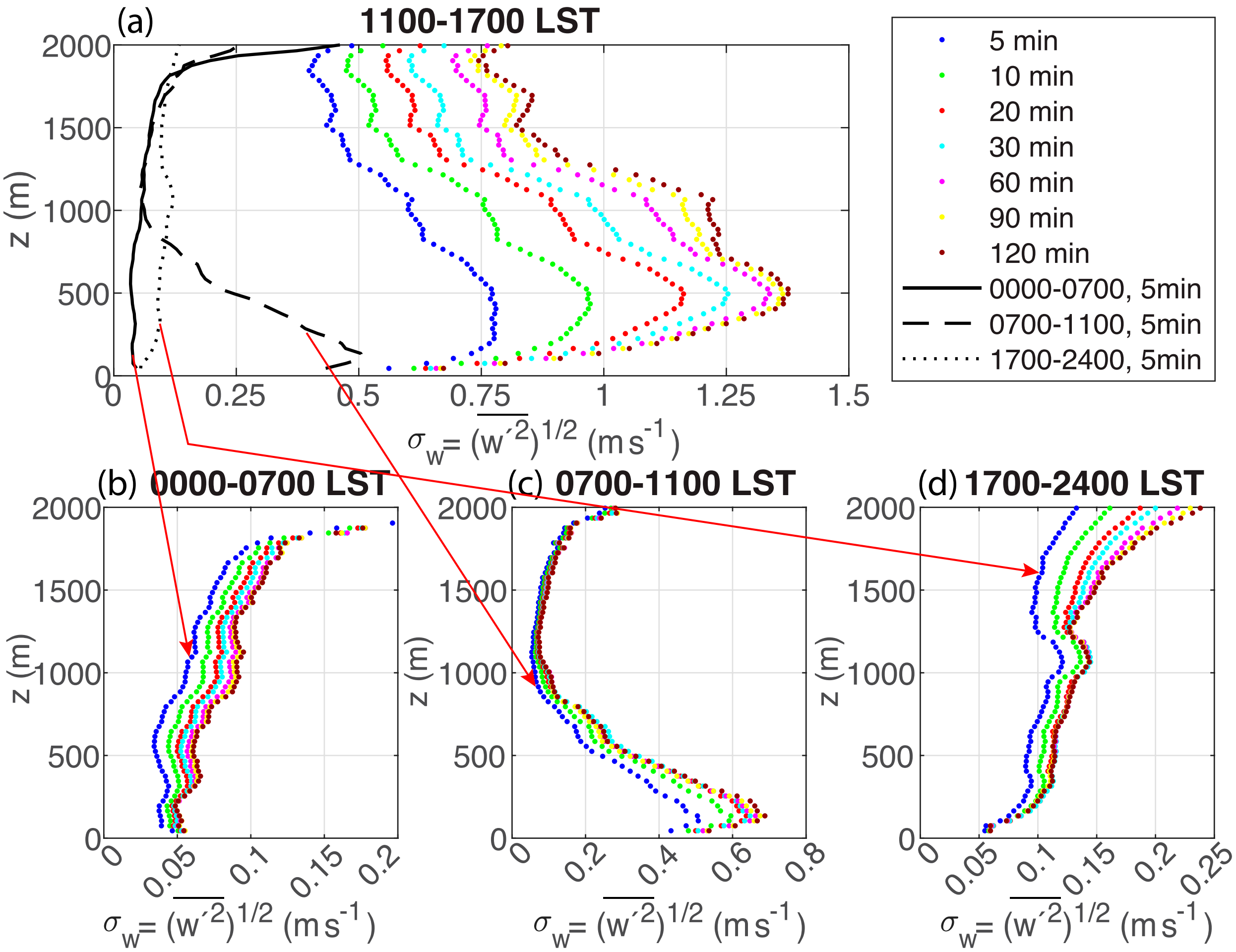

FIG. 9. The standard deviation of the vertical motion $\sigma_w = (\overline{w'^2})^{1/2}$ as a function of height z and the data segment lengths for σ_w from 5 to 120 min marked with different colors for the four time periods specified by the vertical black lines in Fig. 8. For easy comparison of the change of σ_w between the different time periods, the 5-min σ_w in (b), (c), and (d) are plotted as the black curves in (a).

found $\overline{w'^2}$ did not vary significantly with height in the near-neutral marine boundary layer. The observational analyses in the literature imply that the vertical variation of $\overline{w'^2}$ is commonly observed; the hydrostatic equilibrium could only occur when the atmosphere is nearly neutral.

We then investigate characteristics of $\partial\overline{w'^2}/\partial z = \partial\sigma_w^2/\partial z$ in the ABL for the same four time periods (Fig. 10). We first compare the magnitude of $\partial\overline{w'^2}/\partial z$ with the estimated temporal variation of mean vertical motion, $\partial\overline{w}/\partial t$. Because of the surface heating for generating turbulent eddies in the lower CBL, the strongest $\partial\overline{w'^2}/\partial z$ is about 4×10^{-3} m s^{-2} in the lower CBL under the strong convective condition (Fig. 10a). The observed largest $\overline{w}$ at any height below 2 km during any of the four time periods is approximately -0.28 m s^{-1} during the convective period, which is much less than the vertical oscillation of the most energetic large turbulent eddies ($\sigma_w \sim 1.4$ m s^{-1}) during the same period. The largest temporal variation of $\overline{w}$, $\partial\overline{w}/\partial t$, is about 4×10^{-6} m s^{-2} between the convective period of 1100–1700 LST and the evening period of 1700–2400 LST. Clearly, $\partial\overline{w}/\partial t$ is much less than $\partial\overline{w'^2}/\partial z$ on this convective day. Therefore, the acceleration of vertical motions is dominated by large-eddy turbulent motions, which further confirms the close relationship between the hydrostatic imbalance and $\partial\overline{w'^2}/\partial z$ at least in the ABL.

The positive $\partial\overline{w'^2}/\partial z$ at the lower CBL increases with increasing surface heating up to the maximum σ_w height of ~500 m implies that the tower observed daytime $-(\partial\overline{p}/\partial z + \overline{\rho}g) > 0$ can extend from the surface up to ~500 m during the convective period. The systematic vertical decrease of $\partial\overline{w'^2}/\partial z$ with its zero value at the maximum σ_w in the CBL implies that the hydrostatic imbalance switches sign at the elevation of the maximum σ_w, which is further examined in section 4b. Due to the decreasing strength of the most energetic turbulent eddies at night, the magnitude of $\partial\overline{w'^2}/\partial z$ is reduced significantly, but never approaches zero steadily during the night, which could be due to the atmospheric stratification and the background wind shear. The seemingly zero $\partial\overline{w'^2}/\partial z$ between 1000 and 1700 m in the early morning in Fig. 10c is due to the relatively large range of the horizontal scale for covering the increasing $\partial\overline{w'^2}/\partial z$ near the surface during the early CBL development. The dominant

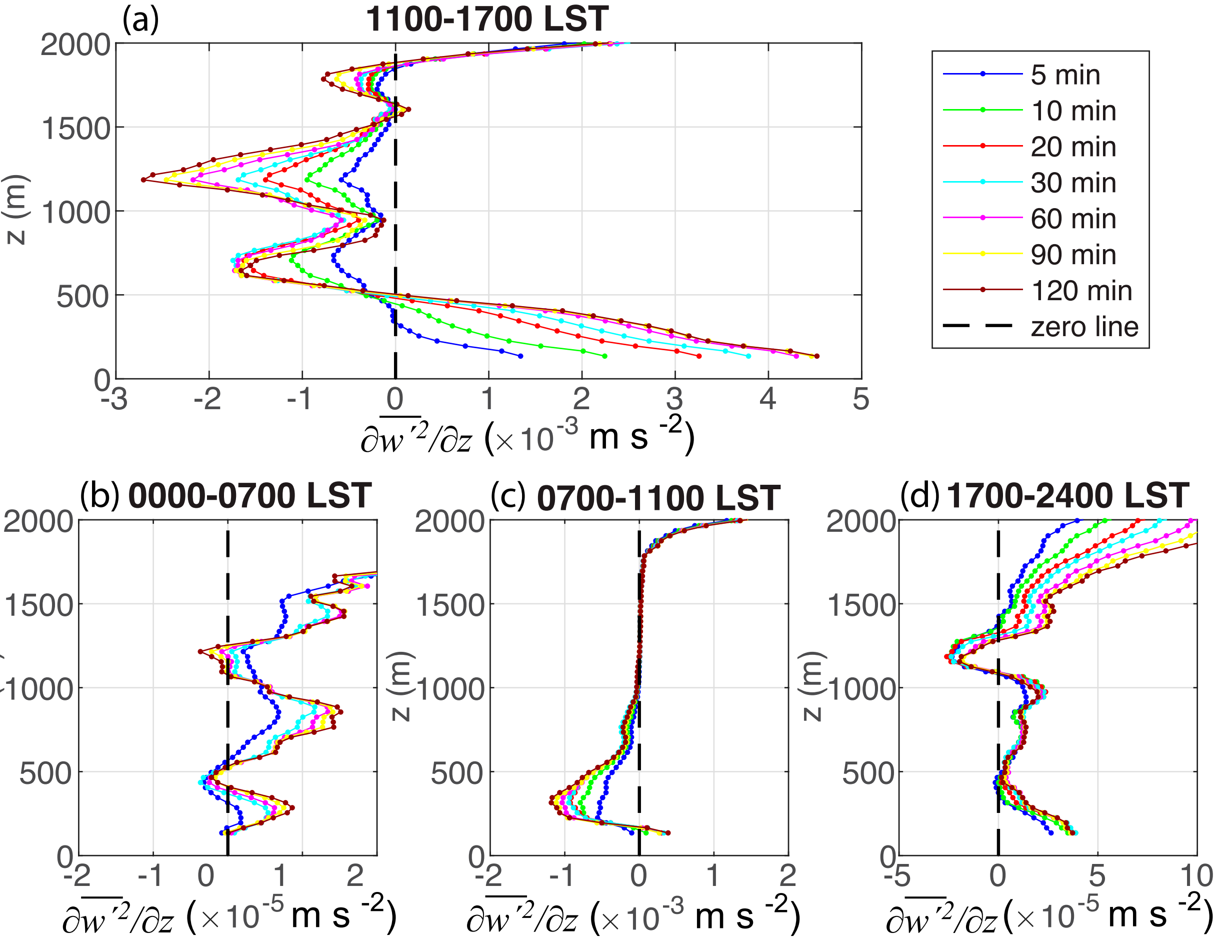

FIG. 10. The vertical derivative of $\overline{w'^2}$, $\partial \overline{w'^2}/\partial z$ as a function of height z and the data segment lengths from 5 to 120 min. The black dashed line in each panel marks the zero $\partial \overline{w'^2}/\partial z$, which approximately corresponds to the hydrostatic equilibrium of the mean atmospheric state. Note that the magnitude of the nighttime $\partial \overline{w'^2}/\partial z$ in (b) and (d) is reduced by two orders of magnitude from its daytime value.

positive $\partial \overline{w'^2}/\partial z$ at night suggests the nighttime reestablishment of the relatively large vertical pressure gradient $\partial p/\partial z > 0$. The vertical oscillation of $\partial \overline{w'^2}/\partial z$ throughout the night (Figs. 10b,d) implies the sensitivity of hydrostatic imbalance to heterogeneous weak vertical air density transfer or the lack of the physical mechanism for achieving hydrostatic equilibrium even with the weak mechanical generation of turbulence in the stable atmosphere above the surface layer.

b. *Understanding the hydrostatic imbalance in the convective boundary layer*

To investigate vertical variations of the hydrostatic imbalance, $-(\partial\overline{p}/\partial z + \overline{\rho}g)$, beyond the tower layer, we analyze GPS radiosonde and Doppler radar observations on the sunny convective day of 3 June 2018 during GRAINEX when the maximum downward solar radiation is about 1000 W m^{-2} and thermally generated turbulence and the hydrostatic imbalance are expected to be relatively large (Fig. 12). On this day, large turbulent eddies generated by the surface heating are captured by vertical velocity observed with the 915 MHz Doppler radar (Fig. 11a) described in section 2d. Due to the 30-min data sampling for the radar observation in comparison with the 10-s lidar observation at LAFO, we examine the vertical variation of σ_w over three periods: the entire day, the daytime between 0800 and 1800 LST, and the most convective period, 1100–1600 LST (Fig. 11b). Similar to the lidar observation at LAFO, the largest σ_w in the ABL is observed during the most convective period. The smallest σ_w for the entire day is due to small σ_w values at night. Different from the convective day at LAFO, the maximum σ_w is weaker and the altitude of the maximum σ_w is higher. The smaller σ_w could be due to reduced w values in each 30-min data sampling window, which is much larger than the 10-s sample window from the Doppler lidar. The higher altitude of the maximum σ_w is expected due to the large maximum downward solar radiation of 1000 W m^{-2} for this case in comparison with 800 W m^{-2} for the LAFO case. The relatively strong wind above the CBL on this day could also play a role in enhancing vertical heat transfer (Fig. 12f).

We then investigate the GPS radiosonde to study the vertical variation of the hydrostatic imbalance throughout the

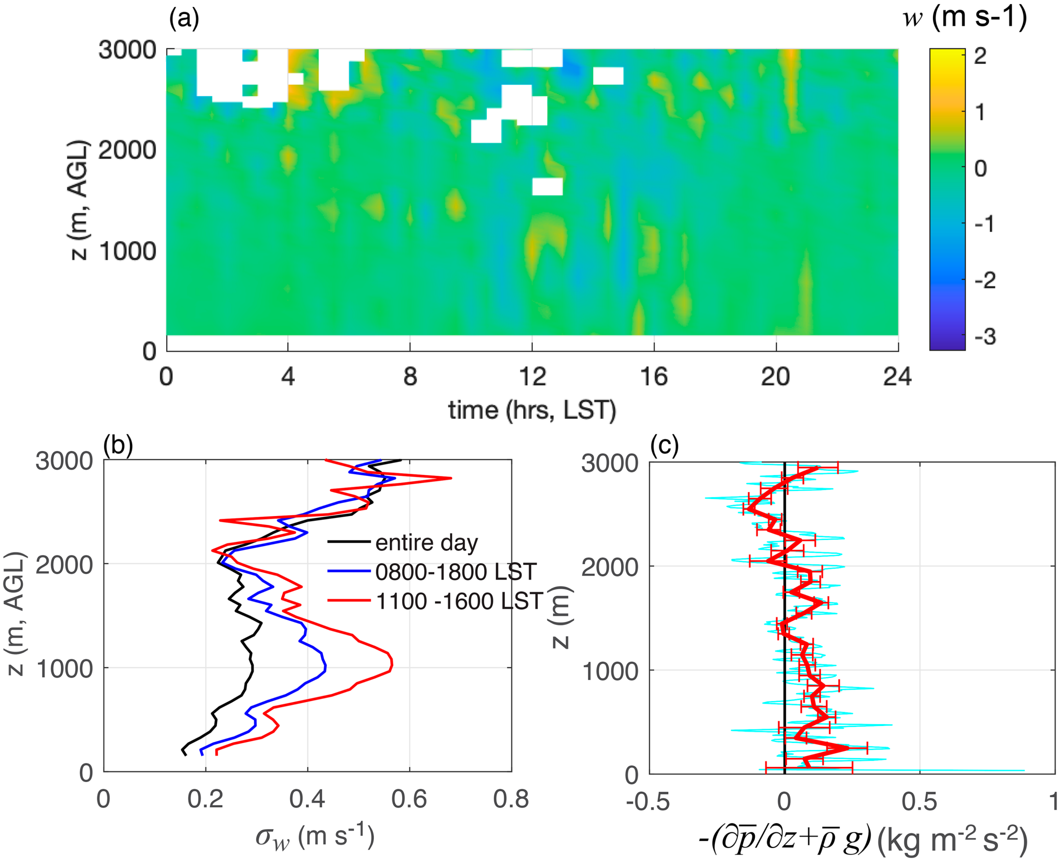

FIG. 11. (a) The vertical velocity w from the 915-MHz radar profiler, (b) the standard deviation of w, i.e., σ_w, as a function of height for different time windows, and (c) the estimated hydrostatic imbalance $-(\partial\overline{p}/\partial z + \overline{\rho}g)$ during the most convective period as a function of height on 3 Jun during GRAINEX. The cyan curve in (c) is composited from three GPS soundings at 1100, 1300, and 1500 LST at every 10 m, the thick red curve is the bin-averaged cyan curve at every 100 m, and the thin red horizontal lines represent the standard deviation of the hydrostatic imbalance within each bin. The vertical black line in (c) is the zero line.

ABL. With the progress of the GPS radiosonde technology, the sonde altitude is obtained independently using the GPS system without relying on the hydrostatic equilibrium assumption. Air pressure is independently measured as well during GRAINEX. In the early morning, the surface layer at 0500 and 0700 LST was visibly stable in the increasing potential temperature θ with height and the decreasing water-vapor specific humidity q with height within the SBL as well as the vertical wind direction change within and above the SBL (green and red profiles in Figs. 12b,c,g). The nearly vertically invariant θ, water-vapor specific humidity q, and wind speed (ws) in the upper ABL at these early-morning hours indicate that there is a well-mixed layer above the stable layer, which could be due to the previous convective daytime mixing upstream somewhere or the relatively strong wind above in the early morning (Fig. 12f). By 0918 LST, the bottom layer of the ABL switches from stable to unstable until sometime after sunset around 1700 LST when the surface layer switches back to being stable again. The impact of the surface heating on the air temperature increase is evident in the consistently increasing θ near the surface until about 1700 LST.

The air density ρ is observed to decrease steadily with height throughout the day with the relatively large ρ in the shallow SBL during the early-morning hours (green and red profiles in Fig. 12d). To examine the air density variation in the bottom 3000-m layer of the atmosphere as a result of the temporal variation of the surface heating beyond its seemingly linear decrease with height (Fig. 12d), we investigate the air density deviation $\delta\rho$ from the linear mean of all the soundings in the 3000-m layer for the day (marked with red circles in Fig. 12d). We find that $\delta\rho$ in the lower CBL decreases steadily with time from 0500 to 1700 LST due to thermal expansion following the increasing surface air temperature (Fig. 12i). The impact of the vertical transport of the surface low-density air to the CBL is evident in the growth of the increasing negative $\delta\rho$ layer associated with the newly developed warm moist air with a nearly constant θ and q within the layer (Figs. 12b,c,i). The increasing $\delta\rho$ with height from being negative to positive during the convective period indicates the decreasing impact of the surface heating on the air density reduction. The consistency between the significant reduction of $\delta\rho$ below 1000 m and the maximum σ_w at 1000 m during the

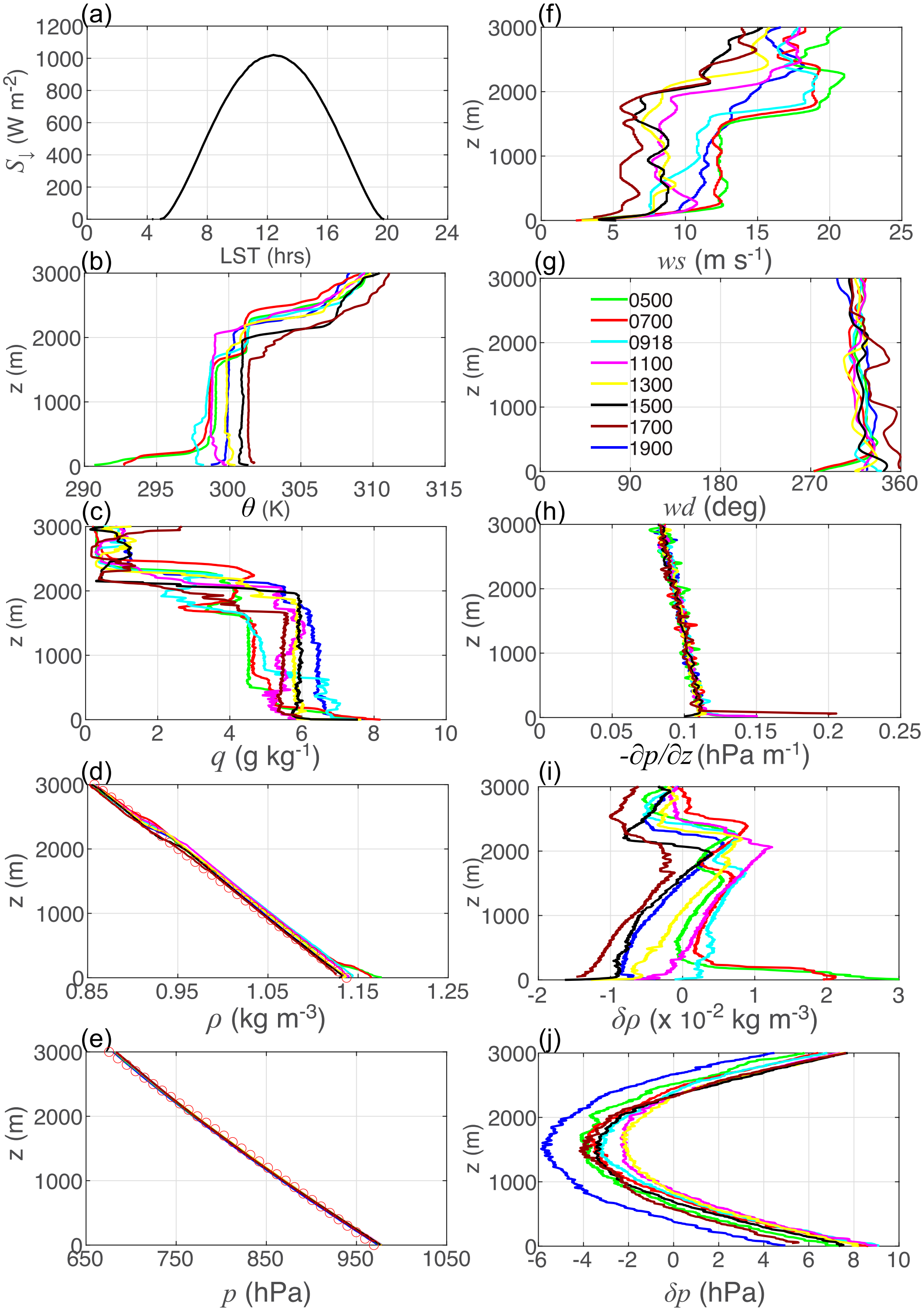

FIG. 12. On the sunny day of 3 Jun 2018 during GRAINEX as shown in (a) the $S_\downarrow$, the development of the CBL is captured by profiles of (b) θ, (c) q, (d) ρ, (e) p, (f) ws, (g) wd, and (h) the estimated vertical pressure gradient $-\partial p/\partial z$. The local launching time for each sounding is labeled in (g). To better view the vertical variation of ρ with time, the deviation $\delta\rho$ of each ρ profile from its linear mean of all the soundings marked with red circles in (d) is plotted in (i). Similarly, the linearly fitted p from all the soundings is marked with red circles in (e), and the deviation δp of each p profile from the fitted linear line is plotted in (j).

most convective time evinces contribution of thermally generated large turbulent eddies to the vertical variation of air density and the consequent change of hydrostatic imbalance.

Similar to the vertical variation of air density, the observed air pressure seems to decrease with height at a constant rate throughout the day (Fig. 12e). However, the deviation of each pressure profile, δp, relative to its linear daily mean within the bottom 3000-m of the atmosphere (marked with red circles in Fig. 12e) reveals that δp varies with height implying that the vertical air pressure decreasing rate is not constant within the 3000-m layer (Fig. 12j). The opposite change of δp with height in the upper and lower half of the 3000-m layer suggests that the positive value of $-\partial p/\partial z$ is larger in the lower half than in the upper half. Additionally, the stronger positive δp at the surface than at 3000-m during the convective time indicates that the decreasing rate of $-\partial p/\partial z$ is larger near the surface than above. That is, neither $-\partial p/\partial z$ nor the vertical variation of $-\partial p/\partial z$ is constant. The variation of the negative δp in the middle of the 3000-m layer from the least negative value at 1300 LST to the most negative one at 1900 LST indicates the contribution of the vertical density flux to the vertical pressure variation. Although both ρ and p seem to decrease linearly with height, the significant vertical variation of $\delta\rho$ in comparison with the vertical variation of δp demonstrates the different impacts of the surface heating/cooling on ρ and $-\partial p/\partial z$, which further confirms the contribution of the background air pressure to the pressure change in the atmosphere. The directly calculated $-\partial p/\partial z$ using the sounding data indicates that $-\partial p/\partial z$ indeed decreases with height steadily with a possible sharp decrease near the surface (Fig. 12h). The small oscillation of $-\partial p/\partial z$ in Fig. 12h is probably due to the GPS altitude accuracy of ±5 m.

We then estimate the hydrostatic imbalance $-(\partial\overline{p}/\partial z + \overline{\rho}g)$ for the most convective period using the calculated air density $\overline{\rho}$ and $-\partial\overline{p}/\partial z$ at 1100, 1300, and 1500 LST (Fig. 11c). Because of the relatively large $-\partial\overline{p}/\partial z$ and the relatively small $\overline{\rho}$ near the surface under convective conditions, the hydrostatic imbalance $-(\partial\overline{p}/\partial z + \overline{\rho}g)$ is relatively large and positive near the surface. As $-\partial\overline{p}/\partial z$ decreases with height, and the impact of the vertical turbulent transfer of air density on the gravity force $-\overline{\rho}g$ becomes increasingly important in determining the hydrostatic imbalance with height. Because of the significant reduction of air density at the bottom half of the 3000-m layer as shown in the vertical extend of the most negative $\delta\rho$ at 1500 and 1700 LST when the accumulated impact of the surface heating reaches to its daily maximum (Fig. 12i), the hydrostatic imbalance $-(\partial\overline{p}/\partial z + \overline{\rho}g)$ is positive in the layer below the vertical maximum σ_w where σ_w increases with height (Figs. 11b,c). Above it, the most negative $\delta\rho$ starts to increase with height as the surface-heating-generated turbulence reduces its intensity for its upward transport of the low air density air, $-(\partial\overline{p}/\partial z + \overline{\rho}g)$ becomes negative and σ_w decreases with height. The sign change of $\partial\sigma_w/\partial z$ from being positive in the lower CBL to being negative in the upper CBL is consistent with the observed decrease of $-(\partial\overline{p}/\partial z + \overline{\rho}g)$. The height of $-(\partial\overline{p}/\partial z + \overline{\rho}g) = 0$ depends on accuracies of the sounding measurements especially the GPS height. As the hydrostatic imbalance becomes weak, the vertical momentum dissipation becomes important for reducing $\partial\overline{w'^2}/\partial z$ especially when turbulence intensity is large (e.g., Banta et al. 2007). Additionally, as the air density decreases with height, the required momentum force for the acceleration of vertical motions becomes smaller, which challenges measurement accuracies.

The above analyses of the vertical variation of $\overline{w'^2}$ using the Doppler lidar and radar observations and the vertical variation of the hydrostatic imbalance using the GPS radiosonde observations further confirm the tower observation on the contribution of the vertical turbulent density transport to the development of hydrostatic imbalance (section 3d). That is, the hydrostatic imbalance is due to the vertical air density transfer by the most energetic large turbulent eddies associated with the diabatic surface heating/cooling and wind shear. Because turbulence is constantly generated by the independent energy source of surface heating/cooling and wind shear and reduced by ceaseless energy dissipation as a result of air viscosity and air movement, the vertical velocity variance, $\overline{w'^2}$, varies spatially and temporally. The hydrostatic imbalance is the consequence of the vertical turbulent air density transfer on mainly the air density change but also on the vertical pressure-gradient change. Therefore, the steady equilibrium between the positive vertical pressure-gradient force $-\partial\overline{p}/\partial z$ and the negative gravity force $-\overline{\rho}g$ is not observed even under weak turbulence in the stable atmosphere. Due to the dominant role of the hydrostatic imbalance of the mean atmospheric state in the vertical momentum balance, the vertical variation of $\overline{w'^2}$ is a good indicator for the hydrostatic imbalance. The consistent vertical variation of $\overline{w'^2}$ and the hydrostatic imbalance also implies that the vertical growth of the most energetic turbulent eddies is determined by the development of the hydrostatic imbalance. The contribution of the convective turbulent mixing to the hydrostatic imbalance in the CBL is schematically summarized in Fig. 13.

5. Summary and conclusions

The atmospheric hydrostatic imbalance of the mean state $-(\partial\overline{p}/\partial z + \overline{\rho}g)$ and its contribution to the acceleration of vertical motions are investigated by analyzing in situ tower observations from CASES-99, Doppler lidars measurements at LAFO, as well as GPS radiosondes and Doppler radar observations from GRAINEX in the ABL under clear-sky conditions. Based on the vertical momentum balance, the hydrostatic imbalance is the driving force for the acceleration of vertical velocity motions that consist of both mean and turbulent motions while the remaining force, the vertical momentum dissipation, consumes environment momentum. The ABL observations demonstrate that vertical variations of large-eddy vertical turbulent motions $\partial\overline{w'^2}/\partial z$ dominates the acceleration of vertical motions and the averaged vertical velocity $\overline{w}$ and its temporal variation $\partial\overline{w}/\partial t$ are negligibly small under horizontally homogeneous convective conditions. Consequently, $\partial\overline{w'^2}/\partial z$ is well related to the hydrostatic imbalance $-(\partial\overline{p}/\partial z + \overline{\rho}g)$ and their close relationship is independently validated in the tower layer and throughout the entire ABL.

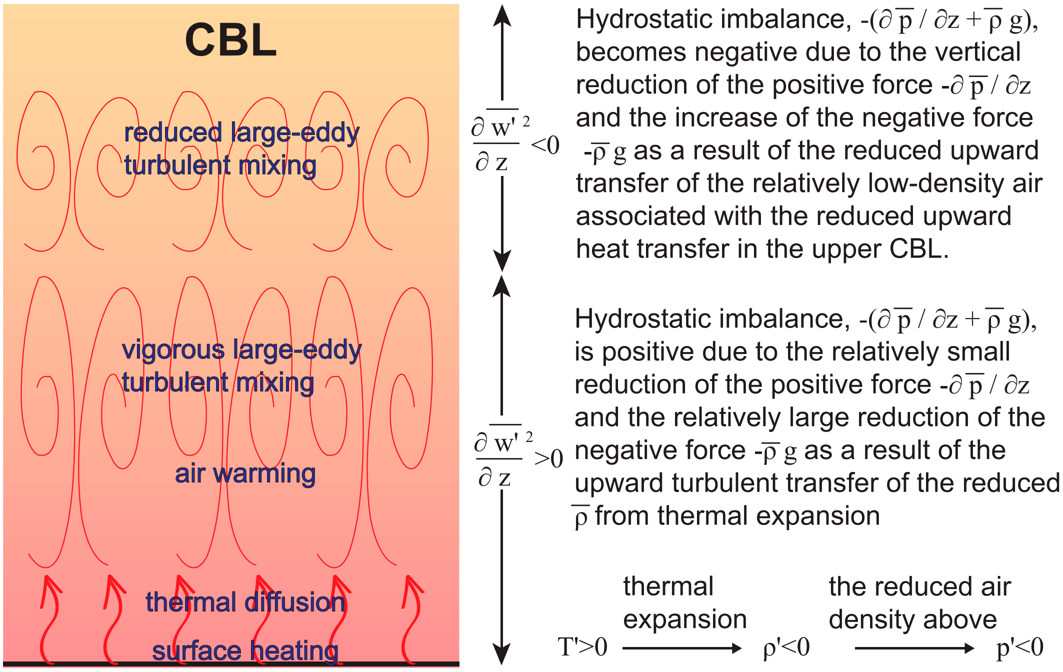

FIG. 13. Schematic summary of the development of the hydrostatic imbalance for the sign change of $\partial\overline{w'^2}/\partial z$ in the CBL by large-eddy turbulent mixing as a result of the surface heating.

The development of the hydrostatic imbalance is observed to be due to turbulent transfer of diurnally varying air density in response to diurnally varying surface temperature through thermal expansion/contraction, which is independent of air compressibility defined at constant temperature. Because the most energetic turbulent eddies are generated by the environmental thermal forcing through surface heating/cooling under clear-sky conditions and/or by mechanical forcing through wind shear, their sizes reflect the environmental forcing scales. These eddies can transport diurnally varying air density well into the ABL under convective conditions. The variation of the hydrostatic imbalance is mainly influenced by changing air density due to the relatively large background $-\partial\overline{p}/\partial z$ although the vertical turbulent transfer of air density impacts both the negative gravity force $-\overline{\rho}g$ and the positive vertical pressure-gradient force, $-\partial\overline{p}/\partial z$.

The vertical variation of the hydrostatic imbalance is also observed to be consistent with the vertical variation of $\partial\overline{w'^2}/\partial z$. Due to the impact of the surface drag and turbulence generation in the ABL, $\overline{w'^2}$ is observed to increase with height throughout the day and to consistently decrease with height only in the upper CBL due to the significant reduction of upward heat transport in turbulence generation. The sign change of $\partial\overline{w'^2}/\partial z$ with height in the CBL is consistent with the sign change of the estimated hydrostatic imbalance due to the steady vertical decrease of the large background $-\partial\overline{p}/\partial z$ and the significant vertical variation of air density as a result of the large upward transport of low-density air in the lower CBL. At night, the hydrostatic imbalance implied from the relatively small vertical variation of $\partial\overline{w'^2}/\partial z$ is significantly reduced due to the lack of strong wind shear in the residual layer above the SBL. However, under nighttime strong wind conditions, the strong upward transport of high-density air from thermal contraction due to the cooling air is observed to contribute more increase to $-\partial\overline{p}/\partial z$ than $-\overline{\rho}g$, such that the positive hydrostatic imbalance force $-(\partial\overline{p}/\partial z + \overline{\rho}g)$ is even larger than its daytime value. Because of ceaseless turbulence in the ABL even under calm stable conditions and the sensitivity of the hydrostatic imbalance to vertical transport of air density, steady adjustment toward the hydrostatic equilibrium is not observed even in the relatively calm nighttime residual layer above the SBL.

The observation study of the development of the hydrostatic imbalance has significant implications for understanding hydrostatic imbalance at large spatial and temporal scales. Thermal expansion/contraction plays a key role in air density changes and the consequent hydrostatic imbalance through the vertical transport of varying air density by large turbulent eddies. The most energetic active turbulent eddies are constantly generated by independent energy sources of surface heating/cooling and wind shear, and their scales are determined by strength and spatial distributions of the environmental forcing, which are much larger than that have been traditionally investigated. Although the size of the most energetic turbulent eddies responsible for developing the hydrostatic imbalance may be still much less than grid sizes of large-scale numerical models, contribution of those turbulent eddies to large spatial and temporal scale hydrostatic imbalance is through their large spatial and temporal distributions in response to their large generation scales such as the vast Earth surface and the continuous diurnal variation of solar radiation. Hydrostatic imbalance cannot be simply adjusted to the hydrostatic equilibrium with ceaseless turbulence generation in the stratified atmosphere, stable or unstable, but can be reduced to a small value when turbulence intensity is relatively small. Because of the critical role of vertical transports of air mass, momentum, and energy for understanding changing atmospheric dynamics and thermodynamics, further investigation of hydrostatic imbalance in the atmosphere especially for cloud development is needed.

Acknowledgments. We thank Drs. Otavio Acedevo and Felipe D. Costa for their feedback and discussions and anonymous reviewers for their thoughtful and constructive comments. Author Sun is supported by National Science Foundation Grant AGS-2203248 and AGS-2231229 for this work. The CASES-99 and GRAINEX data are provided by the NSF NCAR Earth Observing Laboratory (EOL; https://data.eol.ucar.edu/) under the sponsorship of the National Science Foundation.

Data availability statement. The field dataset used in this study is from the NSF UCAR/NCAR EOL, as cited in section 2 and obtained online (https://doi.org/10.5065/D6ZS2TWW, https://doi.org/10.5065/D6WH2NV0, and https://doi.org/10.26023/5Z74-JHT9-JT0X). The data at these sites are freely accessible to the public. The LAFO lidar dataset is available online (https://doi.org/10.5281/zenodo.10213602).

APPENDIX

The Vertical Momentum Balance in the Turbulent Atmosphere

For a two-dimensional flow of a horizontal motion V in the x direction and a vertical motion of w in the z direction, the vertical momentum balance equation can be expressed in terms of the acceleration of vertical motions as (e.g., Stull 1988; Garratt 1992; Sun 2019):

$$\rho\frac{dw}{dt} \equiv \rho\left(\frac{\partial w}{\partial t} + V\frac{\partial w}{\partial x} + w\frac{\partial w}{\partial z}\right) = -\left(\frac{\partial p}{\partial z} + \rho g\right) + \mu\left(\frac{\partial^2 w}{\partial x^2} + \frac{\partial^2 w}{\partial z^2}\right). \tag{A1}$$

Because the atmosphere is approximately an ideal gas and incompressible (the air volume does not change significantly with varying air pressure under a constant air temperature), the air continuity equation can be expressed as

$$\frac{\partial V}{\partial x} + \frac{\partial w}{\partial z} = 0. \tag{A2}$$

Applying Eq. (A2) to Eq. (A1), dw/dt can be expressed as

$$\rho\frac{dw}{dt} \equiv \rho\left[\frac{\partial w}{\partial t} + \frac{\partial(wV)}{\partial x} + \frac{\partial(w^2)}{\partial z}\right] = -\left(\frac{\partial p}{\partial z} + \rho g\right) + \mu\left(\frac{\partial^2 w}{\partial x^2} + \frac{\partial^2 w}{\partial z^2}\right). \tag{A3}$$

We then perform Reynolds averaging to Eq. (A3) by decomposing any variable ϕ to $\phi \equiv \overline{\phi} + \phi'$, where $\overline{\phi}$ represents the Reynolds average of ϕ and ϕ' represents the perturbation of ϕ from its Reynolds average $\overline{\phi}$. Because the Reynolds average represents a simple box-mean average, $\overline{\phi'} = \overline{\phi - \overline{\phi}} = \overline{\phi} - \overline{\overline{\phi}} = 0$. Thus, ϕ^2 can be expressed as $\overline{\phi^2} = \overline{(\overline{\phi} + \phi')^2} = \overline{\phi}^2 + \overline{\phi'^2}$. Reynolds decomposing Eq. (A3)/ρ, using the Taylor expansion

$$\frac{1}{\rho} = \frac{1}{\overline{\rho} + \rho'} \approx \frac{1}{\overline{\rho}}\left(1 - \frac{\rho'}{\overline{\rho}}\right), \tag{A4}$$

with the assumption of $|\rho'/\overline{\rho}| \ll 1$, and Reynolds averaging the decomposed Eq. (A3)/ρ, we have

$$\begin{aligned}\overline{\rho}\left[\frac{\partial\overline{w}}{\partial t} + \frac{\partial(\overline{w}\,\overline{V} + \overline{w'V'})}{\partial x} + \frac{\partial(\overline{w}^2 + \overline{w'^2})}{\partial z}\right] \\ = -\left(\frac{\partial\overline{p}}{\partial z} + \overline{\rho}g\right) + \mu\left(\frac{\partial^2\overline{w}}{\partial x^2} + \frac{\partial^2\overline{w}}{\partial z^2}\right) + \overline{\frac{\rho'}{\overline{\rho}}\left(\frac{\partial p'}{\partial z} + \rho' g\right)} \\ - \frac{\mu}{\overline{\rho}}\overline{\rho'\left(\frac{\partial^2 w'}{\partial x^2} + \frac{\partial^2 w'}{\partial z^2}\right)}.\end{aligned} \tag{A5}$$

Assuming $|\partial p'/\partial z| \ll \partial\overline{p}/\partial z$ and $|\rho'/\overline{\rho}| \ll 1$ (see section 3c for the discussion of the approximations), the third term on the right-hand side of Eq. (A5) would be much smaller than the first term. Assuming the surface and the ambient flow are horizontally homogeneous, any turbulent-eddy-induced horizontal motions would be horizontally divergent/convergent following the continuity equation. Thus, horizontal variations of any turbulent motions would oscillate around zero. Therefore, $\partial\overline{\phi}/\partial x$ would be approximately negligibly small. Thus, Eq. (A5) becomes

$$\overline{\rho}\left[\frac{\partial\overline{w}}{\partial t} + \frac{\partial(\overline{w}^2 + \overline{w'^2})}{\partial z}\right] = -\left(\frac{\partial\overline{p}}{\partial z} + \overline{\rho}g\right) + \mu\frac{\partial^2\overline{w}}{\partial z^2} - \frac{\mu}{\overline{\rho}}\overline{\rho'\frac{\partial^2 w'}{\partial z^2}}. \tag{A6}$$

Because the ambient large-scale vertical motion is normally negligibly small, $\overline{w}$ represents the averaged turbulent motion. Averaging up and down vertical motions of turbulent eddies generated by either horizontally homogeneous surface heating/cooling or wind shear, $\overline{w}$ would be much smaller than $(\overline{w'^2})^{1/2}$ (see lidar observations in section 4a). Thus, Eq. (A6) would be approximated as

$$\overline{\rho}\frac{\partial(\overline{w'^2})}{\partial z} = -\left(\frac{\partial\overline{p}}{\partial z} + \overline{\rho}g\right) - \frac{\mu}{\overline{\rho}}\overline{\rho'\frac{\partial^2 w'}{\partial z^2}}. \tag{A7}$$

REFERENCES

Acevedo, O. C., and Coauthors, 2018: Monitoring the micrometeorology of a coastal site next to a thermal power plant from the surface to 140 m. *Bull. Amer. Meteor. Soc.*, **99**, 725–738, https://doi.org/10.1175/BAMS-D-17-0134.1.

Adrian, R. J., R. T. D. S. Ferreira, and T. Boberg, 1986: Turbulent thermal convection in wide horizontal fluid layers. *Exp. Fluids*, **4**, 121–141, https://doi.org/10.1007/BF00280263.

Angevine, W. M., H. Jiang, and T. Mauritsen, 2010: Performance of an eddy diffusivity–mass flux scheme for shallow cumulus boundary layers. *Mon. Wea. Rev.*, **138**, 2895–2912, https://doi.org/10.1175/2010MWR3142.1.

——, J. Olson, J. J. Gristey, I. Glenn, G. Feingold, and D. D. Turner, 2020: Scale awareness, resolved circulations, and practical limits in the MYNN–EDMF boundary layer and shallow cumulus scheme. *Mon. Wea. Rev.*, **148**, 4629–4639, https://doi.org/10.1175/MWR-D-20-0066.1.

Arakawa, A., 2004: The cumulus parameterization problem: Past, present, and future. *J. Climate*, **17**, 2493–2525, https://doi.org/10.1175/1520-0442(2004)017<2493:RATCPP>2.0.CO;2.

——, and C. S. Konor, 2009: Unification of the anelastic and quasi-hydrostatic systems of equations. *Mon. Wea. Rev.*, **137**, 710–726, https://doi.org/10.1175/2008MWR2520.1.

Atlas, R. L., C. S. Bretherton, P. N. Blossey, A. Gettelman, C. Bardeen, P. Lin, and Y. Ming, 2020: How well do large-eddy simulations and global climate models represent observed boundary layer structures and low clouds over the summertime Southern Ocean? *J. Adv. Model. Earth Syst.*, **12**, e2020MS002205, https://doi.org/10.1029/2020MS002205.

Banta, R. M., R. K. Newsom, J. K. Lundquist, Y. L. Pichugina, R. L. Coulter, and L. Mahrt, 2002: Nocturnal low-level jet characteristics over Kansas during CASES-99. *Bound.-Layer Meteor.*, **105**, 221–252, https://doi.org/10.1023/A:1019992330866.

——, L. Mahrt, D. Vickers, J. Sun, B. B. Balsley, Y. L. Pichugina, and E. J. Williams, 2007: The very stable boundary layer on nights with weak low-level jets. *J. Atmos. Sci.*, **64**, 3068–3090, https://doi.org/10.1175/JAS4002.1.

Bezerra, V. L., and Coauthors, 2021: Near-surface atmospheric turbulence in the presence of a squall line above a forested and deforested region in the central Amazon. *Atmosphere*, **12**, 461, https://doi.org/10.3390/atmos12040461.

Bonin, T. A., P. M. Klein, and P. B. Chilson, 2020: Contrasting characteristics and evolution of southerly low-level jets during different boundary-layer regimes. *Bound.-Layer Meteor.*, **174**, 179–202, https://doi.org/10.1007/s10546-019-00481-0.

Bradshaw, P., 1967: 'Inactive' motion and pressure fluctuations in turbulent boundary layers. *J. Fluid Mech.*, **30**, 241–258, https://doi.org/10.1017/S0022112067001417.

Burns, S. P., and J. Sun, 2000: Thermocouple temperature measurements from the CASES-99 main tower. *14th Symp. on Boundary Layer and Turbulence*, Snowmass, CO, Amer. Meteor. Soc., P9.5, https://ams.confex.com/ams/AugAspen/webprogram/Paper14856.html.

——, J. M. Frank, W. J. Massman, E. G. Patton, and P. D. Blanken, 2021: The effect of static pressure-wind covariance on vertical carbon dioxide exchange at a windy subalpine forest site. *Agric. For. Meteor.*, **306**, 108402, https://doi.org/10.1016/j.agrformet.2021.108402.

Cotton, W. R., G. Bryan, and S. C. Van den Heever, 2010: *Storm and Cloud Dynamics*. Academic Press, 820 pp.

Cuxart, J., G. Morales, E. Terradellas, and C. Yagüe, 2002: Study of coherent structures and estimation of the pressure transport terms for the nocturnal stable boundary layer. *Bound.-Layer Meteor.*, **105**, 305–328, https://doi.org/10.1023/A:1019974021434.

Donner, L. J., 1993: A cumulus parameterization including mass fluxes, vertical momentum dynamics, and mesoscale effects. *J. Atmos. Sci.*, **50**, 889–906, https://doi.org/10.1175/1520-0469(1993)050<0889:ACPIMF>2.0.CO;2.

Dudhia, J., 1993: A nonhydrostatic version of the Penn State–NCAR mesoscale model: Validation tests and simulation of an Atlantic cyclone and cold front. *Mon. Wea. Rev.*, **121**, 1493–1513, https://doi.org/10.1175/1520-0493(1993)121<1493:ANVOTP>2.0.CO;2.

Ecklund, W. L., D. A. Carter, B. B. Balsley, P. E. Currier, J. L. Green, B. Weber, and K. Gage, 1990: Field tests of a lower tropospheric wind profiler. *Radio Sci.*, **25**, 899–906, https://doi.org/10.1029/RS025i005p00899.

Edwards, J. M., A. C. M. Beljaars, A. A. M. Holtslag, and A. P. Lock, 2020: Representation of boundary-layer processes in numerical weather prediction and climate models. *Bound.-Layer Meteor.*, **177**, 511–539, https://doi.org/10.1007/s10546-020-00530-z.

Eliassen, A., and E. Palm, 1960: On the transfer of energy in stationary mountain waves. *Geofys. Publ.*, **22** (3), 1–23.

Foken, T., 1978: The molecular temperature boundary layer of the atmosphere over various surfaces. *Arch. Meteor. Geophys. Bioklimatol.*, **27A**, 59–67, https://doi.org/10.1007/BF02246461.

——, 2017: *Micrometeorology*. 2nd ed. Springer, 362 pp., https://doi.org/10.1007/978-3-642-25440-6.

Garratt, J. R., 1992: *The Atmospheric Boundary Layer.* Cambridge Atmospheric and Space Science Series, Cambridge University Press, 316 pp.

Geiger, R., R. H. Aron, and P. Todhunter, 1995: *The Climate near the Ground*. 5th ed. Harvard University Press, 528 pp.

Högström, U., 1990: Analysis of turbulence structure in the surface layer with a modified similarity formulation for near neutral conditions. *J. Atmos. Sci.*, **47**, 1949–1972, https://doi.org/10.1175/1520-0469(1990)047<1949:AOTSIT>2.0.CO;2.

Hutchins, N., K. Chauhan, I. Marusic, J. Monty, and J. Klewicki, 2012: Towards reconciling the large-scale structure of turbulent boundary layers in the atmosphere and laboratory. *Bound.-Layer Meteor.*, **145**, 273–306, https://doi.org/10.1007/s10546-012-9735-4.

Kaimal, J. C., and J. A. Businger, 1970: Case studies of a convective plume and a dust devil. *J. Appl. Meteor.*, **9**, 612–620, https://doi.org/10.1175/1520-0450(1970)009<0612:CSOACP>2.0.CO;2.

Katul, G. G., J. D. Albertson, M. B. Parlange, C.-I. Hsieh, P. S. Conklin, J. T. Sigmon, and K. R. Knoerr, 1996: The "inactive eddy" motion and the large-scale turbulent pressure fluctuations in the dynamic sublayer. *J. Atmos. Sci.*, **53**, 2512–2524, https://doi.org/10.1175/1520-0469(1996)053<2512:TEMATL>2.0.CO;2.

Krug, D., W. J. Baars, N. Hutchins, and I. Marusic, 2019: Vertical coherence of turbulence in the atmospheric surface layer: Connecting the hypotheses of Townsend and Davenport. *Bound.-Layer Meteor.*, **172**, 199–214, https://doi.org/10.1007/s10546-019-00445-4.

Kuo, H.-L., 1974: Further studies of the parameterization of the influence of cumulus convection on large-scale flow. *J. Atmos. Sci.*, **31**, 1232–1240, https://doi.org/10.1175/1520-0469(1974)031<1232:FSOTPO>2.0.CO;2.

Lenschow, D. H., J. C. Wyngaard, and W. T. Pennell, 1980: Mean-field and second-moment budgets in a baroclinic, convective boundary layer. *J. Atmos. Sci.*, **37**, 1313–1326, https://doi.org/10.1175/1520-0469(1980)037<1313:MFASMB>2.0.CO;2.

——, V. Wulfmeyer, and C. Senff, 2000: Measuring second- through fourth-order moments in noisy data. *J. Atmos. Oceanic Technol.*, **17**, 1330–1347, https://doi.org/10.1175/1520-0426(2000)017<1330:MSTFOM>2.0.CO;2.

——, M. Lothon, S. D. Mayor, P. P. Sullivan, and G. Canut, 2012: A comparison of higher-order vertical velocity moments in the convective boundary layer from lidar with in situ measurements and large-eddy simulation. *Bound.-Layer Meteor.*, **143**, 107–123, https://doi.org/10.1007/s10546-011-9615-3.

Li, J., J. Sun, M. Zhou, Z. Cheng, Q. Li, X. Cao, and J. Zhang, 2018: Observational analyses of dramatic developments of a severe air pollution event in the Beijing area. *Atmos. Chem. Phys.*, **18**, 3919–3935, https://doi.org/10.5194/acp-18-3919-2018.

Li, X., G. Wang, and X. Zheng, 2022: Turbulent/synoptic separation and coherent structures in the atmospheric surface layer for a range of surface roughness. *Bound.-Layer Meteor.*, **182**, 75–93, https://doi.org/10.1007/s10546-021-00643-z.

Mahrt, L., 1986: On the shallow motion approximations. *J. Atmos. Sci.*, **43**, 1036–1044, https://doi.org/10.1175/1520-0469(1986)043<1036:OTSMA>2.0.CO;2.

——, 2010: Variability and maintenance of turbulence in the very stable boundary layer. *Bound.-Layer Meteor.*, **135** (1), 1–18, https://doi.org/10.1007/s10546-009-9463-6.

——, 2011: The near-calm stable boundary layer. *Bound.-Layer Meteor.*, **140**, 343–360, https://doi.org/10.1007/s10546-011-9616-2.

——, 2014: Stably stratified atmospheric boundary layers. *Annu. Rev. Fluid Mech.*, **46**, 23–45, https://doi.org/10.1146/annurev-fluid-010313-141354.

Marusic, I., and J. P. Monty, 2019: Attached eddy model of wall turbulence. *Annu. Rev. Fluid Mech.*, **51**, 49–74, https://doi.org/10.1146/annurev-fluid-010518-040427.

McBean, G. A., and J. A. Elliott, 1975: The vertical transports of kinetic energy by turbulence and pressure in the boundary layer. *J. Atmos. Sci.*, **32**, 753–766, https://doi.org/10.1175/1520-0469(1975)032<0753:TVTOKE>2.0.CO;2.

Morse, C. S., R. K. Goodrich, and L. B. Cornman, 2002: The NIMA method for improved moment estimation from Doppler spectra. *J. Atmos. Oceanic Technol.*, **19**, 274–295, https://doi.org/10.1175/1520-0426-19.3.274.

Olson, J. B., J. S. Kenyon, W. A. Angevine, J. M. Brown, M. Pagowski, and K. Sušelj, 2019: A description of the MYNN-EDMF scheme and the coupling to other components in WRF-ARW. NOAA Tech. Memo. OAR GSD-61, NOAA, 42 pp., https://doi.org/10.25923/n9wm-be49.

Ooyama, K., 1971: A theory on parameterization of cumulus convection. *J. Meteor. Soc. Japan*, **49A**, 744–756, https://doi.org/10.2151/jmsj1965.49A.0_744.

Pandey, A., J. D. Scheel, and J. Schumacher, 2018: Turbulent superstructures in Rayleigh-Bénard convection. *Nat. Commun.*, **9**, 2118, https://doi.org/10.1038/s41467-018-04478-0.

Poulos, G. S., and Coauthors, 2002: CASES-99—A comprehensive investigation of the stable nocturnal boundary layer. *Bull. Amer. Meteor. Soc.*, **83**, 555–581, https://doi.org/10.1175/1520-0477(2002)083<0555:CACIOT>2.3.CO;2.

Prein, A. F., and Coauthors, 2015: A review on regional convection-permitting climate modeling: Demonstrations, prospects, and challenges. *Rev. Geophys.*, **53**, 323–361, https://doi.org/10.1002/2014RG000475.

Rappin, E., and Coauthors, 2021: The Great Plains Irrigation Experiment (GRAINEX). *Bull. Amer. Meteor. Soc.*, **102**, E1756–E1785, https://doi.org/10.1175/BAMS-D-20-0041.1.

Satoh, M., 2014: *Atmospheric Circulation Dynamics and General Circulation Models.* Springer, 730 pp.

Schlichting, H., and K. Gersten, 2000: *Boundary-Layer Theory.* Springer, 801 pp.

Shaw, W. J., and J. A. Businger, 1985: Intermittency and the organization of turbulence in the near-neutral marine atmospheric boundary layer. *J. Atmos. Sci.*, **42**, 2563–2584, https://doi.org/10.1175/1520-0469(1985)042<2563:IATOOT>2.0.CO;2.

Siebesma, A. P., and J. W. M. Cuijpers, 1995: Evaluation of parametric assumptions for shallow cumulus convection. *J. Atmos. Sci.*, **52**, 650–666, https://doi.org/10.1175/1520-0469(1995)052<0650:EOPAFS>2.0.CO;2.

——, P. M. M. Soares, and J. Teixeira, 2007: A combined eddy-diffusivity mass-flux approach for the convective boundary layer. *J. Atmos. Sci.*, **64**, 1230–1248, https://doi.org/10.1175/JAS3888.1.

Skamarock, W. C., and J. B. Klemp, 2008: A time-split nonhydrostatic atmospheric model for weather research and forecasting applications. *J. Comput. Phys.*, **227**, 3465–3485, https://doi.org/10.1016/j.jcp.2007.01.037.

——, ——, M. G. Duda, L. D. Fowler, S.-H. Park, and T. D. Ringler, 2012: A multiscale nonhydrostatic atmospheric model using centroidal Voronoi tesselations and C-grid staggering. *Mon. Wea. Rev.*, **140**, 3090–3105, https://doi.org/10.1175/MWR-D-11-00215.1.

Smith, R. B., 1979: The influence of mountains on the atmosphere. *Advances in Geophysics*, Vol. 21, Academic Press, 87–230, https://doi.org/10.1016/S0065-2687(08)60262-9.

Soares, P. M. M., P. M. A. Miranda, A. P. Siebesma, and J. Teixeira, 2004: An eddy-diffusivity/mass-flux parametrization for dry and shallow cumulus convection. *Quart. J. Roy. Meteor. Soc.*, **130**, 3365–3383, https://doi.org/10.1256/qj.03.223.

Späth, F., and Coauthors, 2023a: The Land–Atmosphere Feedback Observatory: A new observational approach for characterizing land–atmosphere feedback. *Geosci. Instrum. Methods Data Syst.*, **12**, 25–44, https://doi.org/10.5194/gi-12-25-2023.

——, V. Rajtschan, and V. Wulfmeyer, 2023b: Dataset for publication: Investigation of hydrostatic imbalance with field observations (version 1). Zenodo, https://doi.org/10.5281/zenodo.10213602.

Stephens, G. L., 2005: Cloud feedbacks in the climate system: A critical review. *J. Climate*, **18**, 237–273, https://doi.org/10.1175/JCLI-3243.1.

Straka, J. M., R. B. Wilhelmson, L. J. Wicker, J. R. Anderson, and K. K. Droegemeier, 1993: Numerical solutions of a non-linear density current: A benchmark solution and comparisons. *Int. J. Numer. Methods Fluids*, **17** (1), 1–22, https://doi.org/10.1002/fld.1650170103.

Stull, R. B., 1988: *An Introduction to Boundary Layer Meteorology*. Kluwer Academic Publishers, 666 pp.

——, 1993: Review of non-local mixing in turbulent atmospheres: Transilient turbulence theory. *Bound.-Layer Meteor.*, **62**, 21–96, https://doi.org/10.1007/BF00705546.

Sun, J., 2019: Incorporating the work done by vertical density fluxes in both kinetic and thermal energy conservation equations to satisfy total energy conservation. *J. Appl. Meteor. Climatol.*, **58**, 213–230, https://doi.org/10.1175/JAMC-D-17-0350.1.

——, S. K. Esbensen, and L. Mahrt, 1995: Estimation of surface heat flux. *J. Atmos. Sci.*, **52**, 3162–3171, https://doi.org/10.1175/1520-0469(1995)052<3162:EOSHF>2.0.CO;2.

——, and Coauthors, 2002: Intermittent turbulence associated with a density current passage in the stable boundary layer. *Bound.-Layer Meteor.*, **105**, 199–219, https://doi.org/10.1023/A:1019969131774.

——, S. P. Burns, A. C. Delany, S. P. Oncley, T. W. Horst, and D. H. Lenschow, 2003: Heat balance in nocturnal boundary layers during CASES-99. *J. Appl. Meteor.*, **42**, 1649–1666, https://doi.org/10.1175/1520-0450(2003)042<1649:HBITNB>2.0.CO;2.

——, L. Mahrt, R. M. Banta, and Y. L. Pichugina, 2012: Turbulence regimes and turbulence intermittency in the stable boundary layer during CASES-99. *J. Atmos. Sci.*, **69**, 338–351, https://doi.org/10.1175/JAS-D-11-082.1.

——, D. H. Lenschow, L. Mahrt, and C. Nappo, 2013: The relationships among wind, horizontal pressure gradient, and turbulent momentum transport during CASES-99. *J. Atmos. Sci.*, **70**, 3397–3414, https://doi.org/10.1175/JAS-D-12-0233.1.

——, L. Mahrt, C. Nappo, and D. H. Lenschow, 2015: Wind and temperature oscillations generated by wave-turbulence interactions in the stably stratified boundary layer. *J. Atmos. Sci.*, **72**, 1484–1503, https://doi.org/10.1175/JAS-D-14-0129.1.

——, D. H. Lenschow, M. A. LeMone, and L. Mahrt, 2016: The role of large-coherent-eddy transport in the atmospheric surface layer based on CASES-99 observations. *Bound.-Layer Meteor.*, **160**, 83–111, https://doi.org/10.1007/s10546-016-0134-0.

——, E. S. Takle, and O. C. Acevedo, 2020: Understanding physical processes represented by the Monin–Obukhov bulk formula for momentum transfer. *Bound.-Layer Meteor.*, **177**, 69–95, https://doi.org/10.1007/s10546-020-00546-5.

Taylor, M. A., O. Guba, A. Steyer, P. A. Ullrich, D. M. Hall, and C. Eldrid, 2020: An energy consistent discretization of the nonhydrostatic equations in primitive variables. *J. Adv. Model. Earth Syst.*, **12**, e2019MS001783, https://doi.org/10.1029/2019MS001783.

Townsend, A. A., 1976: *The Structure of Turbulent Shear Flow*. 2nd ed. Cambridge University Press, 429 pp.

UCAR/NCAR Earth Observing Laboratory, 2016: 5 minute statistics of ISFF data during CASES-99, version 1.0. UCAR/NCAR Earth Observing Laboratory, accessed 6 May 2016, https://doi.org/10.5065/D6ZS2TWW.

——, 2018: NCAR/EOL quality controlled radiosonde data—ISS2 Rogers Farm Site, version 1.0. UCAR/NCAR Earth Observing Laboratory, accessed 31 October 2022, https://doi.org/10.5065/D6WH2NV0.

——, 2021: NCAR/EOL ISS Radar Wind profiler–ISS2 Rogers Farm Site, version 2.0. UCAR/NCAR Earth Observing Laboratory, accessed 4 November 2022, https://doi.org/10.26023/5Z74-JHT9-JT0X.

Vickers, D., and L. Mahrt, 2006: Contrasting mean vertical motion from tilt correction methods and mass continuity. *Agric. For. Meteor.*, **138**, 93–103, https://doi.org/10.1016/j.agrformet.2006.04.001.

Vömel, H., and W. Brown, 2018: GRAINEX 2018 radiosonde data quality report. UCAR/NCAR–Earth Observing Laboratory, 15 pp.

Wang, Y., and B. Geerts, 2013: Composite vertical structure of vertical velocity in nonprecipitating cumulus clouds. *Mon. Wea. Rev.*, **141**, 1673–1692, https://doi.org/10.1175/MWR-D-12-00047.1.

Wulfmeyer, V., and Coauthors, 2020: The GEWEX Land–Atmosphere Feedback Observatory (GLAFO). *GEWEX Quarterly*, No. 30, International GEWEX Project Office, Silver Spring, MD, 6–11.

Wyngaard, J. C., 2010: *Turbulence in the Atmosphere*. Cambridge University Press, 393 pp.

Xue, M., K. K. Droegemeier, and V. Wong, 2000: The Advanced Regional Prediction System (ARPS)—A multi-scale nonhydrostatic atmospheric simulation and prediction model. Part I: Model dynamics and verification. *Meteor. Atmos. Phys.*, **75**, 161–193, https://doi.org/10.1007/s007030070003.

Zhou, B., S. Sun, J. Sun, and K. Zhu, 2019: The universality of the normalized vertical velocity variance in contrast to the horizontal velocity variance in the convective boundary layer. *J. Atmos. Sci.*, **76**, 1437–1456, https://doi.org/10.1175/JAS-D-18-0325.1.